

Applying a cross-power model for power suppression in FLAMINGO

Ioannis Koutalios,^{1*} Marcel van Daalen,¹

¹Leiden Observatory, Leiden University, P.O. Box 9513, 2300 RA Leiden, The Netherlands

30 June 2024

ABSTRACT

Matter power spectrum can be used to study the way matter clusters in the Universe. Euclid will be able to measure this clustering with unprecedented accuracy, using weak lensing measurements. Thus, it becomes more crucial to be able to produce models with an accuracy of 1% or better in all scales $k < 10h/\text{Mpc}$. In [van Loon & van Daalen \(2024\)](#) a proof-of-concept model that is able to utilize cross-power spectra to connect the power spectrum suppression with the observed baryon fractions in a parameter-free way was presented. The model was able to predict the power suppression for scales $k < 8h/\text{Mpc}$ with an accuracy of at least 2%, in a total of 5 simulations from the cosmo-OWL and BAHAMAS projects. We apply this model to the new **FLAMINGO** suite of large-scale cosmological simulations. We find that the increased resolution and grid size allows us to model the connection between the baryon fraction and retained mass of haloes more accurately which increased the accuracy of the model to 1% for most of the simulations we tested. The many different hydro simulations of **FLAMINGO** with different intensities for the baryonic feedback allow us to test the model in all these cases. We find that in the absence of jets, we are always within 1% of the true power suppression, and otherwise at least within 2%.

Key words: cosmological simulations – power spectrum – cross power model – baryonic feedback – power suppression – centre misalignment

1 INTRODUCTION

The study of the large-scale structure of the Universe is an integral part of modern cosmology, used to study the structure on scales larger than that of a galaxy ([Coil 2013](#)). To explore this topic, astronomers have used N-body simulations and track the evolution and clustering of dark matter ([Springel et al. 2006; Angulo & Hahn 2022](#)). These simulations allow us to study how the small ripples on the almost uniform primordial soup gave birth to the observed filament structure ([Gao & Theuns 2007](#)). The formation of galaxies in this structure happens inside the dark matter haloes ([Wechsler & Tinker 2018; Cooray & Sheth 2002a](#)). These haloes contain matter which is decoupled from the cosmic expansion because of the gravitational bound of the particles inside.

To study the way matter clusters in our Universe we can use the matter power spectrum ([Schneider et al. 2016](#)). On large scales, the linear perturbation theory ([Press & Schechter 1974; Bond et al. 1991](#)) can be used to model the power spectrum with high precision. On smaller scales, however, linear perturbation theory is not enough to describe the collapse of haloes and the formation of galaxies and ends up underestimating the power. The analytical halo model (e.g. [Peacock & Smith 2000; Seljak 2000; Cooray & Sheth 2002b; Tinker et al. 2008; Duffy et al. 2008; Giocoli et al. 2010; Sembolini](#)

[et al. 2011, 2013; Zentner et al. 2013; Mead et al. 2015; Debackere et al. 2020; Mead et al. 2021](#)) is able to provide a more accurate description of the matter power spectrum on these non-linear scales.

One other way of obtaining the power spectrum in these non-linear regions is with the use of cosmological simulations. Full hydrodynamical simulations (e.g. [Schaye et al. 2010; Le Brun et al. 2014; Schaye et al. 2015; McCarthy et al. 2017; Villaescusa-Navarro et al. 2021; Salcido et al. 2023; Schaye et al. 2023; Kugel et al. 2023](#)) are able to take into account the effects of galaxy formation ([Vogelsberger et al. 2020](#)) and have the advantage of being more accurate than any analytical approach. The drawback is the required computation time that can get very high for the resolutions and grid sizes required to make these simulations reliable. A different approach is to use the results of N-body, dark matter only simulations and modify the particle outputs. This method is called baryonification (e.g. [Schneider & Teyssier 2015; Schneider et al. 2019, 2020a,b; Aricò et al. 2020, 2021](#)), and is more efficient than the full hydrodynamical simulations, because dark matter only simulations are less computationally expensive. These different approaches have the same goal of accurately predicting the matter power spectrum in the non-linear regime. A review of all these processes can be found in [Chisari et al. \(2019\)](#).

In hydrodynamical (hydro) simulations, gas gets redistributed in haloes or outside of them through a process known

* E-mail: koutalios@mail.strw.leidenuniv.nl

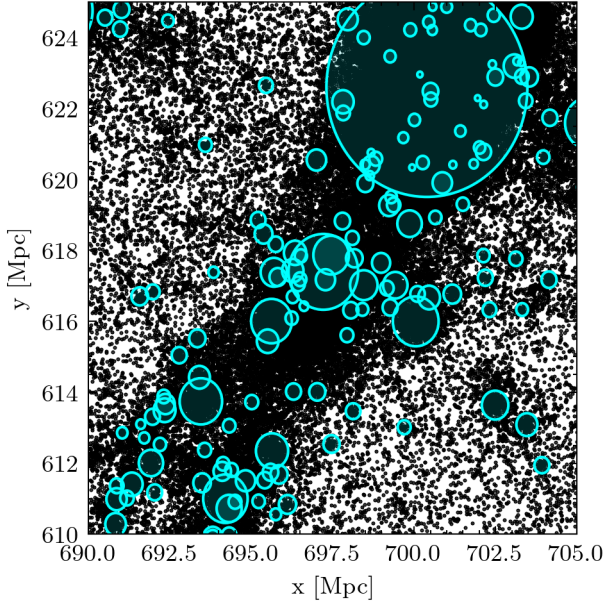


Figure 1. Clustering of mass in the dark matter only simulation of FLAMINGO used in this project. The area shown is a small part (15 Mpc across each dimension) of the full simulation, showing a part of the filament structure. The projection is on the x-y plane, distances are in Mpc. With blue, we plot the projection of the R_{200m} of all the haloes within those limits.

as baryonic feedback. The source of this feedback can be traced to different mechanisms such as stars or supermassive black holes. In van Daalen et al. (2011) it was shown that this will also have an effect in the dark matter of the haloes, through a process called “back-reaction” (Duffy et al. 2010). The power suppression that comes from this feedback can be studied by considering the ratio between the power spectrum in a hydro and a dark matter only simulation that has the same initial conditions (Jing et al. 2006; Rudd et al. 2008).

With the recent launch of Euclid¹ we will be able to measure the matter power spectrum with higher accuracy than ever before (Laureijs et al. 2011; Euclid Collaboration et al. 2019, 2021, 2024). It becomes increasingly more crucial to be able to produce model power spectra to compare with in order to take full advantage of the increased accuracy of the observations (Huterer & Takada 2005; Laureijs 2009; Hearin et al. 2012; Schneider et al. 2016). By comparing data from weak lensing surveys with parameterized models we will be able to infer the cosmological parameters (Bartelmann & Schneider 2001; Joachimi & Bridle 2010; Kilbinger 2015), which will bring more light to the tension between the early and late Universe measurements of those parameters (Verde et al. 2019; Abdalla et al. 2022; Liu et al. 2024).

In van Loon & van Daalen (2024) a proof-of-concept model that uses the cross-power spectra between matter inside the haloes and the full simulation was presented that is able to connect the baryon fractions to power spectrum suppression without introducing any additional parameters. The contributions to the full matter auto-power spectrum from both

within and outside of haloes have been studied in van Daalen & Schaye (2015). The use of the mean baryon fraction to predict power suppression was first explored in van Daalen et al. (2020). In this “resummation” model, the retained mass fraction is used to scale the cross-power spectra of binned haloes based on their mass. The non-halo cross-power contribution to the full auto-power spectrum is also scaled appropriately to account for the conservation of mass. The results for the cosmo-OWLS (Le Brun et al. 2014) and BAHAMAS (McCarthy et al. 2017) simulations show that this model can reproduce the power suppression for all scales $k < 8 h/\text{Mpc}$ with at least 2% accuracy.

In the current work, we want to apply this model to the new FLAMINGO suite of large-scale cosmological simulations (Schaye et al. 2023; Kugel et al. 2023). The increased grid size and resolution of these simulations allow us to more accurately model the connection of the retained mass of haloes to the baryon fraction. Moreover, the number of different variations of the parameters of the feedback mechanisms in the hydro simulations allows us to test the accuracy of the model in these scenarios.

The structure of this paper is as follows. In section 2 we analyze and explain all the different methods we will use throughout this work. There is a detailed explanation of how we use the simulations and obtain our data, and how we use the FFT algorithm to get the power spectra. There is also an extensive analysis of the “resummation” model and how we apply it in FLAMINGO. Then in section 3 we show and discuss the results we obtained in our analysis. We show all the results for the different steps that are needed to apply the model, and then at the end, we show the final performance of the model. Some extra results are shown in appendices A to D, to further investigate certain topics. In all these cases, we discuss the consequences of our results and the decisions we made throughout this work. Finally, in section 4 we sum up all our findings and the different methods we have used and offer some ideas for future research on this topic.

2 METHODS

In this section, we explain all the different methods we used during our analysis.

2.1 Simulations

We use the FLAMINGO simulations (Schaye et al. 2023; Kugel et al. 2023) to study the power suppression in the matter power spectrum. The FLAMINGO simulations are a set of cosmological, large-scale structure simulations and are part of the Virgo consortium for cosmological supercomputer simulations. The resolution of these simulations depends on the number of particles being used. For unresolved processes, such as star or black hole formation, subgrid models are being used. In FLAMINGO the subgrid prescriptions for stellar and AGN feedback are calibrated to the observed low-redshift galaxy stellar mass function and cluster gas fractions in order to guarantee that the simulations are realistic enough for studies of large-scale structures. There is also a use of machine learning for calibration purposes, which is performed independently for the three resolutions being used. For the

¹ www.esa.int/Science_Exploration/Space_Science/Euclid

Simulation	N Particles
Dark Matter Only	1800^3
Fiducial	2×1800^3
Weak AGN	2×1800^3
Strong AGN	2×1800^3
Stronger AGN	2×1800^3
Strongest AGN	2×1800^3
Strong Supernova	2×1800^3
Stronger AGN + Strong Supernova	2×1800^3
Jets	2×1800^3
Strong Jets	2×1800^3

Table 1. List of the different simulations from the **FLAMINGO** suite that we will use in our analysis. The hydrodynamical simulations have the same number of dark matter particles as the dark matter only simulation but also include gas, stars, and black holes.

simulations, the **SWIFT** simulation code (Schaller et al. 2024) was deployed on the Memory Intensive DiRAC facility.

FLAMINGO builds on top of previous simulations like OWLS (Schaye et al. 2010), cosmo-OWLS (Le Brun et al. 2014), EA-GLE (Schaye et al. 2015), and BAHAMAS (McCarthy et al. 2017). The VELOCIRaptor (Elahi et al. 2019) subhalo finder was used to identify structures like haloes and subhaloes in the simulations. For the purposes of the **FLAMINGO** simulation the spherical Overdensity and Aperture Processor (SOAP) tool was developed, which can directly take the output of the VELOCIRaptor to calculate different properties of these structures.

There are different box sizes and resolutions for the **FLAMINGO** simulations. For the purposes of this analysis, we will use the “L1_m9” simulations, which have a box size of 1000Mpc in each dimension and a resolution of 1800^3 particles for the dark matter particles. For each set of simulations, there are multiple hydrodynamical simulations and one corresponding dark matter only simulation. The different hydrodynamical simulations use different mechanisms and/or intensities for the baryonic feedback, which will lead to different power suppression in the matter power spectrum (see section 2.5). The dark matter only simulations can be used as a reference to calculate the power suppression due to the baryonic feedback.

An overview of the different simulations that we will use in our analysis is given in table 1. We have in total 9 different hydrodynamical simulations that we analyze. The fiducial simulation uses the standard intensities for all the feedback mechanisms and is used as the primary model for comparing with all the other simulations. It does not necessarily mean that these values are the most likely to be correct, but they are the best starting point to compare from. Then we have 4 simulations that vary the intensity of the AGN feedback. From weak to strongest, means that less or more gas is ejected from the halo. This is crucial in our analysis as it will have a huge impact on the power suppression that we want to study. The next two simulations use a stronger supernova feedback than the fiducial simulation, with or without a stronger AGN feedback. Finally, the last two simulations use a different implementation of the AGN feedback. The fiducial simulation uses thermal AGN with no jets. In contrast, the jets simulations use AGN jets which distribute the gas that is being ejected in a non-uniform way. They also eject the gas

Parameter	Value
Ω_m	0.306
Ω_Λ	0.694
Ω_b	0.0486
h	0.681
m_b	$1.07 \times 10^9 M_\odot$
m_{CDM}	$5.65 \times 10^9 M_\odot$
M_{CDM}	$6.72 \times 10^9 M_\odot$

Table 2. List of the values of the cosmological and simulation parameters in the simulations we use that are relevant in our work. The density parameters: Ω_m for the total matter, Ω_Λ for the dark energy and Ω_b for the baryonic matter. With h we denote the dimensionless Hubble constant. The masses represent the initial mass of: the baryonic particles m_b , the cold dark matter particles in the hydro simulations m_{CDM} , and the cold dark matter particles in the dark matter only simulations M_{CDM} .

at greater distances, forming the astrophysical jets that we are familiar with from deep sky images.

All the simulations use the fiducial cosmology, which uses the cosmological parameters that are taken from Abbott et al. (2022). In table 2 we give the values of some of the cosmological parameters as well as the initial masses of the baryonic and cold dark matter particles in the dark matter only and hydro simulations. For each simulation, there are multiple snapshots for different values of redshift. In our analysis, we will only use the snapshots that correspond to a redshift of $z = 0$. For a more detailed description of the different simulations and cosmologies used in the **FLAMINGO** suite, we refer to the original paper (Schaye et al. 2023).

2.2 Mass Fractions

The model that we use in this work (section 2.6) requires the scaling of dark matter power spectra (section 2.5) to account for the power suppression that is caused by the baryonic feedback that is present in hydrodynamical simulations. For this purpose, we need to define some useful quantities that we will use when applying the model.

In order to compare the different simulations, we need to be able to match the different haloes in the different simulations of the **FLAMINGO** suite. We are interested in matching haloes for each hydro simulation with the corresponding haloes in the dark matter only simulation. Luckily, this process is already done in **FLAMINGO** by comparing the particle IDs that are part of the haloes in the different simulations. This process is possible due to the starting conditions of the simulations, which are identical for each set of simulations. The result is a matching file that can connect the haloes in the different simulations of the same corresponding box size and resolution. For our purposes, we only use main haloes that match in the different simulations, both ways. This means that the matching file for the hydro simulation should point to the corresponding halo in the dark matter only simulation and vice versa.

The first quantity that we need is the fraction of the mass that is retained in the hydrodynamical simulation, compared with the dark matter only simulation. For a single halo, we can define this quantity as:

$$f_{\text{ret}} = \frac{M_{\text{hydro}}}{M_{\text{DMO}}}, \quad (1)$$

where M_{hydro} and M_{DMO} are the masses of the halo in the hydrodynamical and dark matter only simulations respectively. As it is clear from the equation above, this quantity takes values between 0 and 1, in the presence of mass loss (e.g. due to feedback from stars and AGN). It can also take values greater than 1 if the mass of the halo in the hydrodynamical simulation is greater than the mass of the halo in the dark matter only simulation.

We can also calculate for each halo in a hydrodynamical simulation the fraction of the total mass that is baryonic. This is the baryon fraction inside the halo and is defined as:

$$f_b = \frac{M_{\text{bar}}}{M_{\text{hydro}}} = \frac{M_{\text{gas}} + M_{\text{stars}} + M_{\text{BH}}}{M_{\text{hydro}}}, \quad (2)$$

where M_{bar} is the mass of the baryons in the halo, which consists of gas, stars, and black holes (BH). The range of values for f_b is between 0 and 1, where 0 means that there are no baryons in the halo and 1 means that the halo has no dark matter.

In the absence of any physical processes that affect the concentration of baryons, such as the baryonic feedback, we expect:

$$f_b = \frac{\Omega_b}{\Omega_m}, \quad (3)$$

where Ω_b is the baryon density parameter and Ω_m is the matter density parameter.

In an ideal case, during a process of baryonic feedback, we would only have baryonic mass getting ejected from the haloes. In this scenario, we would be able to use instead of the retained mass fraction, the corrected baryon mass fraction to scale the dark matter only power spectra. The corrected baryon fraction was introduced in [van Loon & van Daalen \(2024\)](#) and is defined as:

$$f_{bc} = \frac{1 - \Omega_b/\Omega_m}{1 - f_b}, \quad (4)$$

where we take into consideration the initial baryon fraction is defined as Ω_b/Ω_m from eq. (3) and that the cold dark matter will be fully retained ($f_{\text{ret}}/f_{bc} = 1$).

The ideal case described above, where $f_{\text{ret}}/f_{bc} = 1$, fails because the dark matter that is present in the haloes will respond to the baryonic feedback, due to the gravitational interaction between the dark matter and the baryons ([van Daalen et al. 2011](#)). The gravitational potential of the halo will change and dark matter, which only interacts gravitationally, will also feel the impact of the baryonic feedback. This will lead to a relaxation of the halo and additional loss of mass, as the potential of the halo gets smaller and some of the dark matter will no longer be bound to the halo.

We can model this effect by mapping the retained mass fraction to the corrected baryon mass fraction. By doing this we are able to use the baryon fraction as a proxy for the retained mass fraction. The accuracy of this mapping will be explored in section 3.2. This is very useful as the baryon fraction can be measured from observations (e.g. [Spergel et al. 2007](#); [Hoekstra et al. 2005](#); [Mandelbaum et al. 2006](#); [Gavazzi et al. 2007](#)), while the retained mass fraction is not available to us, as we have no direct way of measuring it observationally.

2.3 Centre Misalignment

It is crucial for our analysis to have a reliable way of measuring the centre of the haloes. The reason for that is that we define the haloes as all the particles that are within a sphere of an overdensity region, the centre of which lies at the centre of the halo. When analyzing large overdensity regions, small misalignments of the centre of the halo are negligible, as it does not affect much the number of particles that are inside. The same is not true for relatively large misalignments, which can still cause issues in these large regions. This becomes increasingly important when analyzing smaller overdensity regions. In this case, even small misalignments can have a huge impact, as it will completely change the profile of the region we sample the particles from. Near the centre, we expect a more dense region, than on the outskirts of the halo. This means that when we do not sample the particles from the correct region, we will underestimate the number of particles, leading to a wrong estimation of the mass of the halo and its significance in the power spectrum.

For the **FLAMINGO** simulations, the centre of the haloes is defined as the centre of potential and is calculated using the VELOCIRaptor subhalo finder. It does so by calculating the binding energy of every single particle, taking into consideration the gravitational potential and the kinetic energy of the particles. It is then able to find the most bound one, the location of which is defined as the centre of the halo. This way of calculating the centre of the haloes should work perfectly in theory. However, in practice, we have observed several cases of wrong centre estimation. The extent of the problem, the reasons behind it, as well as possible solutions, is still an open question and more people are actively working on it.

Take for example the halo in fig. 2. For the dark matter only simulation (DMO, blue points) we can see that the centre of the halo (red cross) is where we expect it to be, based on the profile of the particles. For the hydrodynamical simulation (gas, dark matter, stars, and black holes with red, green, yellow and black points respectively), however, we can clearly see that the centre (green cross) is misplaced, and does not correspond to the image we see. The centre is far more to the left than what we would expect, based on the positions of the particles in the hydro simulation, and this leads to a wrong estimation of the particles that are inside each overdensity region. In this particular case, we will get less than 10% of the total mass we would get if the centre was correctly placed. It is therefore clear how centre misalignment can have a huge impact on our analysis.

Since it is beyond the scope of this work to develop a new method to calculate the centre of the haloes, that is both reliable and computationally feasible for a large dataset like the **FLAMINGO** simulations, we need to find a way to limit the impact it has on our analysis. We need, therefore, a probe that can tell us whether the centre of a halo is misplaced or not. The final goal of this is to cut out as many of the haloes that have a misaligned center, as possible, without cutting out the haloes that have a properly placed center.

In theory, one could look directly at the values of f_{ret} . If we take the distribution of the values of f_{ret} for the different haloes, we would expect that the haloes that have a misaligned centre would be on the outliers of the distribution, on either side. If the misalignment happens in the hydrodynamical simulations, we would expect that M_{hydro} would be

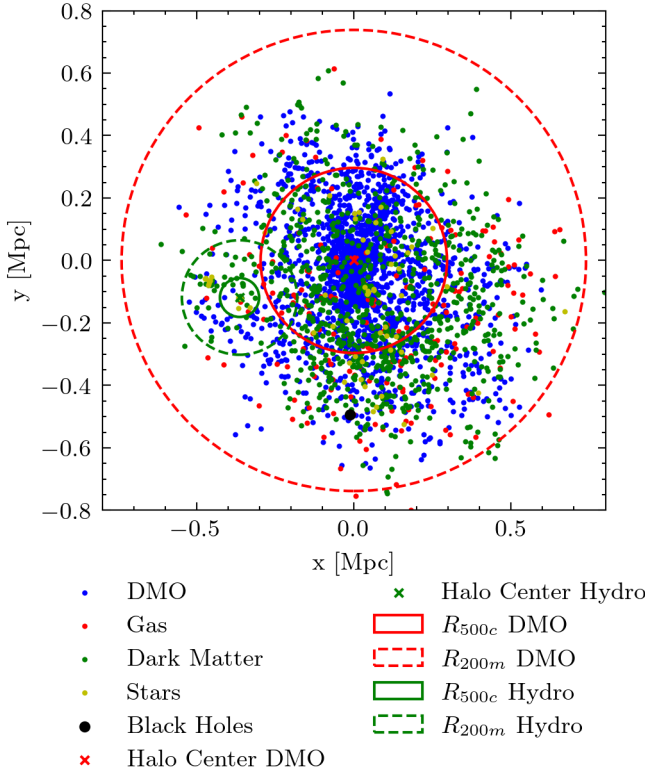


Figure 2. Example of the particle positions for a single halo in the dark matter only simulation (DMO) and the fiducial simulation (Gas, Dark Matter, Stars, Black Holes). We also note the centres of the haloes and two different overdensity regions for both simulations. The projection is done in the x-y plane, distances are in Mpc.

underestimated, leading to a significantly lower value of f_{ret} . On the other hand, if the misalignment happens in the dark matter only simulation, we would expect that M_{DMO} would be underestimated, and f_{ret} would get much higher values. This approach will work in terms of identifying the haloes that have a misaligned centre, but it will also remove all the cases of extremely high baryonic feedback, as well as the cases of extreme increase in M_{hydro} . By doing this we would bias our sample, leading to unreliable results. For this reason, we explore two different probes; the mass profiles of the haloes and the distance of the centre of potential from the centre of mass of the halo.

2.3.1 Mass Profiles

The mass profiles of the haloes can be useful for identifying the haloes that have a misaligned centre. As we have already discussed, the region around the true centre of the halo is usually expected to be denser than the outskirts of the halo. This will give a typical mass profile that starts very steep and then flattens out. On the other hand, if we pick the wrong location for the centre of the halo, these areas will generally be less dense, resulting in an atypical mass profile.

In our analysis, we calculate the mass profiles of the haloes by simply taking the mass of the haloes for different radii. The SOAP tool is able to calculate the mass of the haloes

for different overdensity regions, which we can then use to calculate the mass profiles. We then normalize the mass profiles by the mass of the halo, to make them comparable. By averaging over all the haloes in the simulation, we can then calculate the average mass profile of the haloes. After that, we can take the distance of each mass profile of every individual halo from the average mass profile and create a distribution of these distances. By setting a threshold for the distance, we can then cut out those haloes. The results can be found in section 3.1.1.

We also explore how the mass profiles are connected with the distance between the centres of potential for the dark matter only and the fiducial simulation. In principle we expect the two centres to have a certain distance between each other, it is possible, however, that great distances can be an indicator of some centre misalignment in either the dark matter only or the fiducial simulation. Of course in order to be able to compare these distances for different haloes we need to normalize them by the radius of a certain reference region for each halo. For that purpose, we use the R_{200m} , which we define in sections 2.4 and 2.6.

2.3.2 Centre of Mass

One other potential probe for detecting haloes with a centre misalignment is the distance of the centre of potential from the centre of mass of the halo. The centre of mass is defined as:

$$\vec{r}_{\text{cm}} = \frac{\sum_i m_i \vec{r}_i}{\sum_i m_i}, \quad (5)$$

where m_i is the mass of each particle and \vec{r}_i is the position of each particle.

In FLAMINGO, the centre of mass is calculated using the SOAP tool and the Friends-of-Friends (FoF) haloes. The two centres are not expected to coincide, as they use a different definition, they should however be close to each other. If the centres are far apart, it could be an indication of a centre misalignment. It is important to always compare normalized distances as we should expect larger haloes to have greater distance between the two centres. For that, we always normalize with the radius of a reference region (R_{200m}). If we calculate these normalized distances for all of the haloes, we can then create a distribution and explore the outliers. A threshold can then be set to cut out those haloes. The results are shown in section 3.1.2.

2.4 Definition of Haloes and Bins

In the FLAMINGO simulations, the haloes can be defined as a collection of particles that are gravitationally bound to each other. This is enabled by the VELOCIRaptor subhalo finder, which is able to identify the haloes in the simulations. VELOCIRaptor utilizes the Friends-of-Friends (FoF) algorithm to get members of the haloes and then uses a gravitational unbinding algorithm to identify which of the particles are not actually gravitationally bound to the halo and remove them. This way of defining the haloes is, however, not really useful for real-world applications, as there is no way of determining which particles are bound to a real halo.

In order to make the haloes more useful for our analysis, we need to define them in a similar way to what we are able to

measure from observations. The information we have available in an observation is the number of particles that are within a certain sphere, which we define as a halo. We can also make a distinction between different overdensity regions, which can be relative to the critical density ρ_c or relative to the mean density $\Omega_m \rho_c$. We can follow a similar approach for the **FLAMINGO** simulations, by defining the haloes as all the particles that are within a sphere of a certain overdensity region. With this approach, we can better utilize the simulations to match the observations.

This process is not done automatically by the **FLAMINGO** simulations nor by the VELOCIRaptor subhalo finder and the SOAP tool. Therefore, we need to perform those calculations ourselves. In theory one could very naively find all the centres of the different haloes and then calculate the distance of each particle from the centre, selecting only the particles that are within a certain radius. Using this approach, however, is computationally unfeasible, as it would require a lot of time to calculate the distance of every particle from each centre. The **SWIFTsimIO** module (Borrow & Borisov 2020; Borrow & Kelly 2021) is able to read the output of the **FLAMINGO** simulations and can be used to divide the simulation into boxes. When we select the centre of a certain halo, we can then only consider the particles that are within the corresponding box (or sometimes multiple neighbouring boxes). This is a much more efficient way of selecting the particles that are within a certain halo, as it requires much less computational time. Using the **SWIFTsimIO** module this way was not possible, because of some limitations in the module. We therefore had to draw inspiration from the module and write our own code to perform the same task.

Now that we are able to define the haloes in an appropriate way, we can split the haloes into different bins based on their total mass. In our analysis, we always split the haloes into 10 different bins, which are equally spaced in logarithmic space. We use the mass of each halo as it is given by the M_{200m} property of the haloes, which is the mass of all the particles that are within the overdensity region of $200\Omega_m \rho_c$. We use this metric even when we are defining the haloes with a different overdensity region, as a way to keep the bins consistent. Previous work (van Loon & van Daalen 2024) has used the M_{500c} region for the same purpose, but we consider the M_{200m} region to be a more reliable metric, as it is a larger overdensity region and therefore less sensitive to effects like centre misalignment or others. The bins start from a minimum mass of $M_{200m} = 10^{11} M_\odot$ and reach a maximum mass of $M_{200m} = 10^{16} M_\odot$ with an equal logarithmic spacing. The range of all the different bins we use in our analysis is shown table 3.

2.5 Power Spectra

The power spectrum can be used to describe the distribution of matter in the Universe. It measures the density fluctuations on different scales, which can be used to study the large-scale structure of the Universe. Under the hood, the power spectrum is the Fourier transform of the correlation function of matter and will be denoted as $P(k)$. The wavenumber given by $k = 2\pi/\lambda$, with λ being the physical scale. The power spectrum can be calculated as:

$$P(k) = \langle \delta(\vec{k}) \tilde{\delta}(\vec{k}) \rangle, \quad (6)$$

Bin	Min $\log_{10}(M/M_\odot)$	Max $\log_{10}(M/M_\odot)$
1	11.0	11.5
2	11.5	12.0
3	12.0	12.5
4	12.5	13.0
5	13.0	13.5
6	13.5	14.0
7	14.0	14.5
8	14.5	15.0
9	15.0	15.5
10	15.5	16.0

Table 3. List of the different bins we use in our analysis. We give the \log_{10} value of the minimum and maximum mass divided by the solar mass (M_\odot).

where $\delta(\vec{k})$ is the Fourier transform of the density field $\delta(\vec{x})$, $\tilde{\delta}(\vec{k})$ is the complex conjugate of $\delta(\vec{k})$ and the brackets denote the ensemble average. The density field is defined as:

$$\delta(\vec{x}) = \frac{\rho(\vec{x}) - \bar{\rho}}{\bar{\rho}}, \quad (7)$$

where $\rho(\vec{x})$ is the density at position \vec{x} and $\bar{\rho}$ is the mean density over the whole simulation box. The shot noise term is always present in the discrete Fourier transform of the density field, we can however subtract it by considering that

$$SN = V \frac{\sum_i m_i^2}{(\sum_i m_i)^2}, \quad (8)$$

where V is the volume of the simulation box, and m_i is the mass of each particle in the simulation. If we are considering a dark matter only simulation, where the mass of all the particles is equal ($m_i = m$), the shot noise term can be further simplified to:

$$SN = \frac{V}{N_{\text{particles}}}. \quad (9)$$

For our analysis, we are interested in two different power spectra; the matter-matter auto-power spectrum and the matter-halo cross-power spectrum. The distinction between the two is that the matter-matter auto-power spectrum is the power spectrum of all the matter in the simulation, while the matter-halo cross-power spectrum cross correlates the matter and the haloes we select each time from the simulation.

Given two different fields A and B , the cross-power spectrum can be calculated as:

$$P_{AB}(k) = \langle \delta_A(\vec{k}) \tilde{\delta}_B(\vec{k}) \rangle, \quad (10)$$

where $\delta_A(\vec{k})$ is the Fourier transform of the density field of field A and $\tilde{\delta}_B(\vec{k})$ is the Fourier transform of the density field of field B . The cross-power spectrum is symmetric, meaning that $P_{AB}(k) = P_{BA}(k)$. In this regard, the auto-power spectrum is just a special case of the cross-power spectrum, where $A = B$.

One must be careful when calculating the shot noise term for the cross-power spectrum, as we only need to consider the particles that are part of both terms in the cross-power spectrum, which is the same as the particles in the haloes.

For both cases, we deploy the **nbodykit** module (Hand et al. 2018) to calculate the power spectra. The module is able to calculate the power spectra using the Fast Fourier Transform (FFT) method (Cooley et al. 1969), which makes it very

efficient for large data sets as is the case for the **FLAMINGO** simulations.

In order to be able to accurately measure the spectrum on a wide range with a satisfying resolution in all scales we employ a technique of folding the real space. We do that by dividing the full box into a number of cubic pieces (we can denote with N the divisions across each dimension) and superimpose them into one, while rescaling the dimensions of the cube to get the original size of the box (multiply the position of each particle by N). We then take the power spectrum and multiply it by the number of divisions across each dimension (N) to get the correct power spectrum. By doing this we are able to measure with precision smaller scales than before (higher values of k) without exponentially increasing the computational time and memory needed. This technique is briefly discussed in Jenkins et al. (1998) while it is also deployed in the original **SWIFT** code which is written in C. For our purposes, we had to adapt the technique in **PYTHON**, by writing our own code. We can repeat this technique for an increasing amount of folds until we get to scales that are shot noise-dominated. By subtracting the shot noise from the power spectrum we are able to push our measurements a bit further, to scales we would not otherwise have access to. In the end, we are always limited by the resolution of the original simulations.

When applying the power spectrum function in our simulations we use a grid size of 256 for the mesh grid used by **nbodykit**. We calculate the power spectrum using the original grid and then we fold 6 times across each dimension. We then increase the number of folds across each dimension in powers of 6, 4 times in total (6, 36, 216, 1296). All of these calculations are done in parallel, using the **multiprocessing** module (McKerns et al. 2012), to further increase the efficiency of the algorithm.

2.6 “Resummation” Model

We follow the model that was first introduced in van Loon & van Daalen (2024) to model the baryonic effect on power suppression. The model is based on the “resummation” of rescaled cross-power spectra and the non-halo term of dark matter only simulations. In dark matter only simulations there are no feedback processes (like AGN) which makes a big difference in the distribution of matter inside the haloes and the resulting power spectra. To account for that one could scale down the mass inside the haloes and increase the mass outside of them. It is however more computationally efficient to scale the power spectra to account for this change in the clustering of matter. In this subsection, we will go through the model and explain how we use it in our analysis.

We will start by defining the notation we will use in the following equations. For continuity, we will be as close as possible to the notation used in van Loon & van Daalen (2024). We denote as P_{mm} the matter-matter auto-power spectrum. Haloes are defined as overdensity regions Δ that can be relative to the critical density ρ_c (as in $\Delta = 500\rho_c$) or relative to the mean density $\Omega_m \rho_c$ (as in $\Delta = 200\Omega_m \rho_c$). Haloes are split into different bins depending on their mass, and we will denote each bin as i . Each halo bin has a fraction of the total mass of the full simulation box, which is denoted as $f_{\text{M},i,\Delta}$. The cross-power spectrum of each halo bin with the matter is denoted as $P_{\text{mh},i,\Delta}$ for the matter-halo power spectrum of halo bin i with overdensity Δ . Similarly, the non-halo cross-

power term is denoted as $P_{\text{mnh},\Delta}$ for the matter-non-halo power spectrum. The Δ term in the subscript of the cross-power terms is used to denote the overdensity region we used to define the haloes, as it will lead to different values for the non-halo term.

Since it is assumed that the cross-power terms of the different halo bins are not normalized with regard to mass, the linear halo bias for the large scales of the haloes in each mass bin can be written as:

$$b_{i,\Delta} = \lim_{k \rightarrow 0} \frac{P_{\text{mh},i,\Delta}(k)}{P_{\text{mm}}(k)}. \quad (11)$$

For our purposes, we will compute the bias for the different halo bins by averaging the values of the above fraction over the small k range of $k < 0.1h \text{ Mpc}^{-1}$.

The auto-power spectrum of each simulation can always be written as the sum of the cross-power spectra of the different halo bins with the matter and the non-halo term:

$$P_{\text{mm}}(k) = \sum_i f_{\text{M},i,\Delta} P_{\text{mh},i,\Delta}(k) + P_{\text{mnh},\Delta}(k). \quad (12)$$

The equation above clearly shows the distinction of the two different contributions to the matter-matter auto-power spectrum; the halo contribution and the non-halo contribution.

When applying the model, we only need to calculate all these values for the dark matter only simulations. We then need to properly rescale the cross-power spectra of the dark matter only simulations to account for the mass loss due to the baryonic effects, such as the feedback from stars and AGN. At the same time, we need to rescale the non-halo term of the dark matter only simulations to account for the conservation of mass.

We can now examine how to rescale the cross-power spectra of the dark matter only simulations, to account for this loss of mass. As we are interested in the large-scale effects that these processes cause, we can safely ignore any changes in the profile of the haloes, such as star formation, and only consider their effects on large scales. In reality, we only need to account for the mass loss by using the fraction of the mass that is retained in the haloes in the hydro simulation relative to the mass of the same halo in the dark matter only simulation, which is denoted as $f_{\text{ret},i,\Delta}$ (eq. (1)). As we have previously mentioned (section 2.2) we map f_{ret} to f_{bc} (eq. (4)), which can be directly observed. The results of the mapping are shown in section 3.2.

We can write the corrected cross-power spectrum of each halo bin with the matter as:

$$P'_{\text{mh},i,\Delta}(k) = f_{\text{ret},i,\Delta} P_{\text{mh},i,\Delta}(k). \quad (13)$$

The mass that gets lost from the haloes is then added to the non-halo term of the dark matter only, which ensures that the total mass of the simulation is conserved. There are many ways to redistribute the mass that gets lost from the haloes to the non-halo term. It is tempting to just add the mass uniformly across the simulation box, but this would be a huge oversimplification as matter outside of the haloes is also clustered, although relatively much less compared with the matter inside the haloes. One other solution would be to just add the mass to a linear power component. However, this is also an oversimplification of the problem and is therefore not sufficient as the matter that gets ejected from the haloes will more likely end up clustering just around the haloes, giving a more significant contribution to the power spectrum than

a linear power component. A more realistic approach would be to add the mass to the non-halo term. This assumes that the mass that was already there had a similar distribution, by clustering more significantly around the haloes. Lastly, we also need to take into account that haloes are biased regions, therefore when we remove mass from them we need to make sure that the power at low values of k can still converge to the initial value. With all these considerations in mind, we can write the corrected non-halo term of the dark matter only simulations as:

$$P'_{\text{mnh},\Delta}(k) = \frac{P'_{\text{mm}}(k) - \sum_i f_{\text{ret},i,\Delta} f_{\text{M},i,\Delta} P_{\text{mh},i,\Delta}(k)}{P_{\text{mm}}(k) - \sum_i f_{\text{M},i,\Delta} P_{\text{mh},i,\Delta}(k)} P_{\text{mnh},\Delta}(k). \quad (14)$$

We can further simplify the equation above by dividing the numerator and the denominator by $P_{\text{mm}}(k)$ and take the low k limit:

$$P'_{\text{mnh},\Delta}(k) = \frac{1 - \sum_i f_{\text{ret},i,\Delta} f_{\text{M},i,\Delta} b_{i,\Delta}}{1 - \sum_i f_{\text{M},i,\Delta} b_{i,\Delta}} P_{\text{mnh},\Delta}(k). \quad (15)$$

We can now rewrite eq. (12) with the corrected cross-power spectra and non-halo term:

$$P'_{\text{mm}}(k) = \sum_i f_{\text{M},i,\Delta} P'_{\text{mh},i,\Delta}(k) + P'_{\text{mnh},\Delta}(k), \quad (16)$$

where P'_{mm} is the corrected matter-matter auto-power spectrum, $P'_{\text{mh},i,\Delta}$ is the corrected matter-halo cross-power spectrum as defined in eq. (13), and $P'_{\text{mnh},\Delta}$ is the corrected matter-non-halo cross-power spectrum as defined in eq. (15).

During this analysis, there was an assumption that was implied, which needs to be corrected. The assumption was that a fixed total matter distribution was maintained when we were cross-correlating. To account for this we need to transform the final total matter power spectrum one last time. We first define the ratio of the corrected matter-matter auto-power spectrum to the dark matter only matter-matter auto-power spectrum as:

$$q_\Delta(k) = \frac{P'_{\text{mm}}(k)}{P_{\text{mm}}(k)}. \quad (17)$$

We can now correct both of the components of the corrected matter-matter auto-power spectrum by multiplying them with the ratio defined in eq. (17):

$$P''_{\text{mm}}(k) = q_\Delta(k) P'_{\text{mm}}(k). \quad (18)$$

The corrected matter-halo cross-power spectrum and the corrected matter-non-halo cross-power spectrum are then defined as:

$$P''_{\text{mh},i,\Delta}(k) = q_\Delta(k) P'_{\text{mh},i,\Delta}(k), \quad (19)$$

$$P''_{\text{mnh},\Delta}(k) = q_\Delta(k) P'_{\text{mnh},\Delta}(k). \quad (20)$$

This concludes the ‘‘resummation’’ model that we will use in our analysis. For a more extensive analysis please refer to the original paper in [van Loon & van Daalen \(2024\)](#). To sum up, we start with a dark matter only simulation and split the haloes into different bins based on their total mass. We then compute the cross-power spectra of the different halo bins with the matter and also calculate the non-halo term. We then rescale each cross-spectrum for the mass that is lost due to the baryonic feedback and redistribute it to

the non-halo term, to satisfy the conservation of mass. We then sum all the corrected halo and non-halo contributions to get the corrected matter-matter auto-power spectrum. We then use it once more to calculate the ratio of the corrected matter-matter auto-power spectrum to the dark matter only matter-matter auto-power spectrum and use it to obtain the final corrected matter-matter auto-power spectrum.

The model can also be used for multiple overdensity regions. If we define two different overdensity regions, Δ_1 and Δ_2 , with $R_{\Delta_1} < R_{\Delta_2}$, we can calculate the fraction of the mass that was removed from Δ_1 but not from Δ_2 as:

$$f_{\text{ret},i,\Delta_1,\Delta_2} = f_{\text{ret},i,\Delta_2} - f_{\text{ret},i,\Delta_1}. \quad (21)$$

We can now analyze the region between the two overdensity regions. We denote with A the region between, that is part of Δ_2 but not in Δ_1 . We can obtain the cross-power contribution of the region A with the matter as:

$$P_{\text{mh},i,A}(k) = \frac{f_{\text{M},i,\Delta_2} P_{\text{mh},i,\Delta_2}(k) - f_{\text{M},i,\Delta_1} P_{\text{mh},i,\Delta_1}(k)}{f_{\text{M},i,\Delta_2} - f_{\text{M},i,\Delta_1}}. \quad (22)$$

We can now calculate the corrected cross-power spectrum of the region A with the matter as:

$$P'_{\text{mh},i,A}(k) = [f_{\text{ret},i,\Delta_2} f_{\text{M},i,\Delta_2} - f_{\text{ret},i,\Delta_1} f_{\text{M},i,\Delta_1}] P_{\text{mh},i,A}(k). \quad (23)$$

We now have the three different regions contributing to the total matter-matter auto-power spectrum; the small overdensity region Δ_1 , the region A between the two overdensity regions, and the region outside of Δ_2 , which is the non-halo term. The first two regions combined are the halo contributions and are the same region as Δ_2 . We can therefore write the corrected cross-power spectrum of each halo bin with the matter, for Δ_2 , as:

$$P'_{\text{mh},i,\Delta_2}(k) = P'_{\text{mh},i,\Delta_1}(k) + P'_{\text{mh},i,A}(k). \quad (24)$$

For the non-halo term (which is the region outside Δ_2), there is no difference in the analysis we previously did, when we considered only one overdensity region. We can therefore use the same equation as in eq. (15) to calculate the corrected non-halo term of the dark matter only simulations.

Finally, we only have to recalculate the ratio of the corrected matter-matter auto-power spectrum to the dark matter only matter-matter auto-power spectrum, as in eq. (17), and use it to correct the corrected matter-matter auto-power spectrum, as in eq. (18). For the individual contributions of the halo bins and the non-halo term, we can once more use the same equations as in eq. (19) and eq. (20) respectively.

The combination of two or multiple overdensity regions can significantly improve the results of the model, as it allows for a more detailed analysis of the mass loss due to the baryonic feedback. Specifically, smaller overdensity regions will give a more accurate representation of the mass loss on high values of k (small scales), while larger overdensity regions will give a better account for the mass loss on low values of k (large scales). The limitations come from the precision and resolution of the simulations, especially on the small scales, and the real-world measurements that we can obtain from the observations.

3 RESULTS

In this section, we explore the results of our analysis and provide an explanation based on theoretical knowledge of cosmology and large-scale structures in the Universe.

3.1 Centre Misalignment

We will start by discussing the results on the issue of centre misalignment. In section 2.3 we described why this problem is crucial in our analysis. We also introduced the two probes we will explore in our analysis and the role f_{ret} plays. We will start by examining the mass profiles of the haloes and then move on to the distance of the centre of potential from the centre of mass of the halo.

3.1.1 Mass Profiles

We calculate the mass profiles for all the different haloes in the fiducial simulation by taking the mass of the haloes for different overdensity regions as described in section 2.3. To make them all comparable we normalize each mass profile by the mean mass of all the different regions. After that, we take the mean over all the haloes to get the mean mass profile. We are then able to calculate the difference between the mass profile of each individual halo with the mean profile and create a distribution of all these differences. To calculate the difference we use:

$$d_{\text{profiles}} = \sum_i \frac{|M_i - \bar{M}_i|}{\bar{M}_i}, \quad (25)$$

where M_i is the mass of each halo at each overdensity region that we use to calculate the mass profiles, \bar{M}_i is the mean mass profile of all the haloes in each region and the summation is over all the overdensity regions being used.

To explore how we can use the mass profiles as a probe for centre misalignment, and if the distances of the centres of potential can help in this, we plot the mass profiles of some of the outliers in fig. 3. At the left panel, we have the mean mass profile of all the haloes in the fiducial simulation and we also plot all the mass profiles of individual haloes that are outliers (2σ above the mean) using the distance of the centres of potential. On the right panel we have the same mean but this time we plot the haloes with a difference from the mean mass profile above 2σ than the mean difference. We also denote the standard deviation of the mean mass profile using the grey area.

It is interesting to note how the mass profiles of the individual haloes on the left panel of fig. 3 are in contrast with the individual haloes on the right panel. For the latter case, we can clearly see that there is something weird with these particular haloes, as we would expect in a case of centre misalignment. We see a big spike of mass in the bigger regions (R_{200m} or R_{50c}) which can be explained if we have the wrong centre. On the other hand, on the left panel, we can also see that there are some cases that have abnormal mass profiles, usually haloes that have a small amount of mass at the smaller regions and a big spike in the middle or right side of the figure, however, most of the cases look relatively normal in terms of their mass profile.

In fig. 4 we can see the distribution of the distances of the mass profiles of all the haloes from the mean. We see a slightly

skewed distribution, which can be justified by the potential existence of cases of misaligned centres that make some of the mass profiles deviate more from the mean. We define 2σ as the threshold after which we consider the halo to be an outlier for this probe, for further exploration.

We also calculate the distance between the centres of potential for the dark matter only and the fiducial simulation, again as described in section 2.3. For normalization, we use the R_{200m} , similar to the previous analysis. We then create a distribution of these distances and examine the outliers.

We can see the results in fig. 5. The distribution is very slightly skewed, which, again, might indicate that there are some cases of centre misalignment, that can make the two centres of potential to have greater distances. Once more, we define the 2σ distance from the mean of the distribution as the limit after which we consider the halo to be an outlier for this probe.

We now switch our focus mainly to the difference between the mass profiles from the mean mass profile. Following the discussion in section 2.3 we want to see if having a very different mass profile from the average, will translate into some abnormal values in f_{ret} . For that, we create a distribution of the f_{ret} values of all the haloes and compare it with the same distribution for the outliers from the mass profiles as shown in fig. 4. The results can be seen in fig. 6. On the left panel, we have the distributions as we described, while on the right panel, we take the density distributions to normalize both of them and make it easier to compare.

As we can see in the right panel of fig. 6, the distribution of the outliers is slightly more skewed, and is significantly wider compared with the distribution for all the haloes. This means that it includes relatively more outliers of either high or low values of f_{ret} . From the left panel, however, it is clear that we are still unable to get most of the outliers which is not ideal.

As a last result, we want to see if the outliers we detected with all the different methods so far are able to find the same haloes. To visualize that we use a Venn diagram with three circles, one for the outliers in the distance between the centres of potential, one for the outliers in the mass profiles and one for the outliers in f_{ret} . For this instance, outliers in f_{ret} are defined as the haloes that have $f_{\text{ret}} > \bar{f}_{\text{ret}} + 2\sigma$. This means that we only consider the haloes that have an abnormally high value of f_{ret} and not the ones on the low side of the spectrum. We find the results in fig. 7. As we can see there is not an agreement between the different methods. From all the outliers using the mass profiles, we can calculate the percentage of the haloes that are also outliers in f_{ret} as 4.76%. The same percentage can be calculated for the outliers using the distances of the centres of potential and the f_{ret} as 8.81%, which is still only a small minority. We can finally consider the case of combining the two and finding how many correspond to a high value in f_{ret} , but the percentage of 7.55% is worse than only using the distance of the centres of potential.

In appendix A we include some additional results that are not shown in this section. Figures A1 and A2 are the mass distributions of different halo populations for 2 different overdensity regions (200m and 500c respectively). The distributions for the two regions show many similarities, there is, however, an interesting secondary peak for the 500c region in the distribution of the outliers in the mass profiles. This can be explained if this selection includes many haloes with centre misalignment.

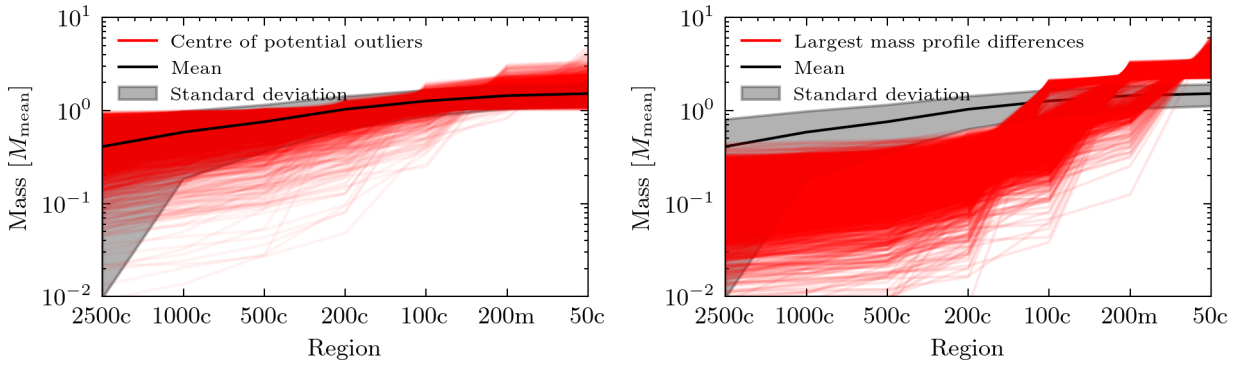


Figure 3. Left panel: Average mass profile of the haloes for the fiducial simulation, with the shaded region denoting the standard deviation. The mass profiles are taken by calculating the mass of the haloes for different overdensity regions and then normalizing them by the mean mass of the halo. We also plot with red all the haloes that have a difference from the average of the distribution of the distances between the centres of potential of the dark matter only and the fiducial simulation above 2σ from the mean. Right panel: Same as the left panel, but with red we plot the haloes that have a difference from the average mass profile 2σ and above the average difference.

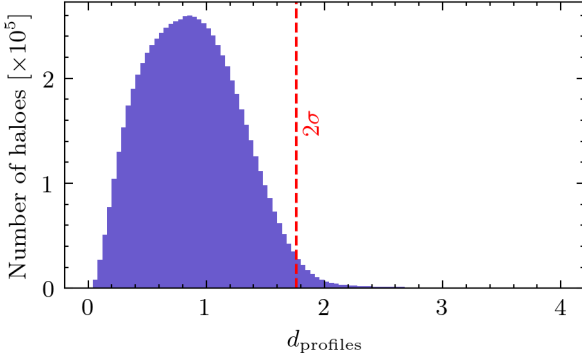


Figure 4. The distribution of the difference between the mass profile of each individual halo and the mean mass profile of all the haloes. All the mass profiles are normalized using the mean mass of all the regions. The difference is calculated by taking the distance of each point of the mass profile from the respecting point of the mean mass profile as shown in eq. (25). With the red line, we note the 2σ distance from the mean of the distribution, which is our cut-off point for identifying outliers using this probe.

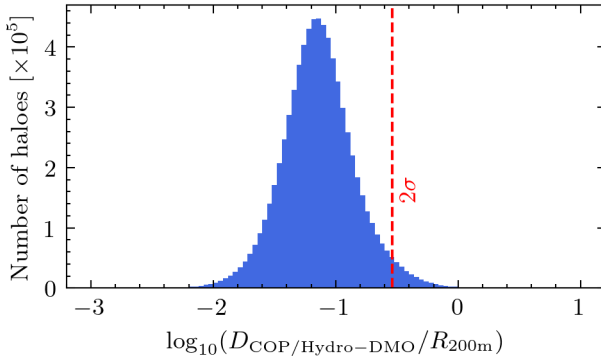


Figure 5. The distribution of the \log_{10} distances between the centres of potential of the dark matter only and the fiducial simulation. With the red line, we note the 2σ distance from the mean of the distribution, which is our cut-off point for identifying outliers using this probe.

With all that in mind, it becomes crucial that we further explore a different probe for detecting centre misalignment in our simulations.

3.1.2 Centre of Mass

We now switch our focus to a different probe. As we discussed in section 2.3 we can use the distance between the centre of potential and the centre of mass as a way to identify outliers and potentially, cases of centre misalignment. It is important that we do this for both the dark matter only and the hydro (in this case the fiducial) simulation. After taking the distances for all the haloes, we can create two separate distributions, one for the dark matter only and one for the fiducial. We can find those results in figs. 8 and 9 respectively.

The two distributions in figs. 8 and 9 are very similar. They are both slightly skewed which can potentially be explained by the existence of haloes with centre misalignment. In both cases, we use the 2.5σ distance from the mean of each distribution to define the outliers.

We now want to test if the outliers we identified using the distances between the centre of potential and the centre of mass are indeed cases of centre misalignment. To test that we will once again try to see how many of these outliers have also abnormal values of f_{ret} . We can do that with two Venn diagrams, where in both cases we plot a circle for each of the outliers of the two distributions. In the first diagram, we also plot a circle for the haloes with high values of f_{ret} (miscentred in DMO, see section 2.3), while on the other for the low values (miscentred in hydro). The results can be seen in fig. 10. Note that we identify the outliers in the two distributions for the distance between the centre of potential and the centre of mass as the haloes that are above 2.5σ from the mean, while for the f_{ret} we only use 2σ .

The picture we get in fig. 10 is much better than in fig. 7. This time we have more haloes that were identified using this probe to also have either very high or low values of f_{ret} which is an indication that we are indeed able to detect many cases of centre misalignment. As we were expecting, outliers in the dark matter only simulation, correspond more to the high values of f_{ret} than the small ones. This makes sense as we know that cases of centre misalignment will lead to

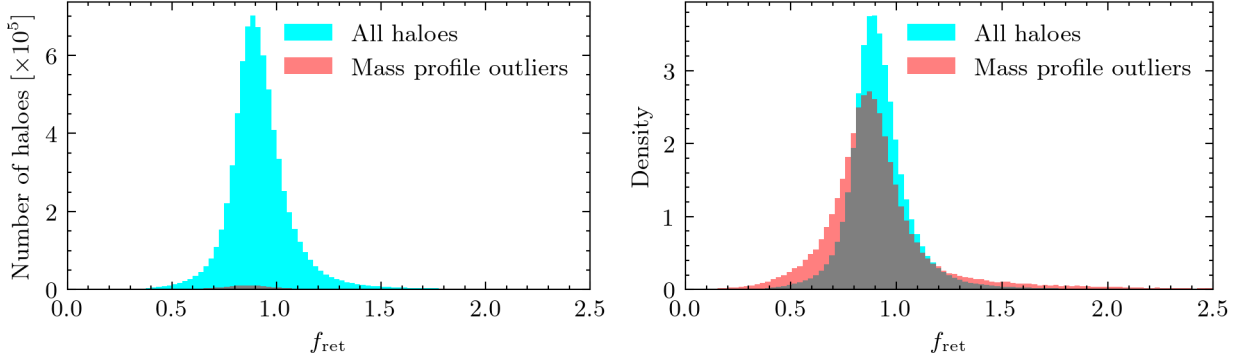


Figure 6. Left panel: Distribution of the values of f_{ret} . With blue, we have all the haloes and with red, only the haloes that have a difference from the average mass profile of more than 2σ . Right panel: Same as the left panel, but both distributions are normalized, to make them easy to compare. From the right panel we can see that with our probe, we are able to select more outliers relative to the distribution of all haloes. However, as we can see from the left panel, we are not able to catch most of them.

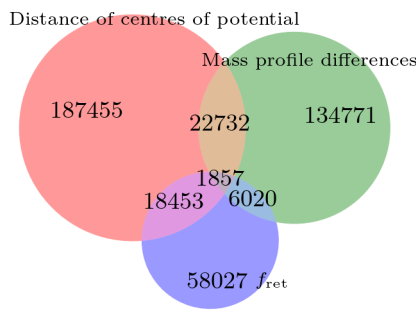


Figure 7. Venn diagrams of haloes that are identified as outliers by some of the probes we use to detect the centre misalignment. We include haloes that are identified as outliers by the mass profiles of the haloes, haloes that are identified as outliers by the distance of the centre of potential of the dark matter only simulation with the centre of potential of the fiducial simulation and the values of f_{ret} .

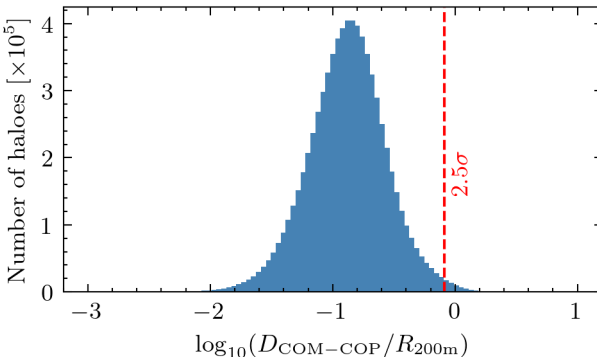


Figure 8. The distribution of the \log_{10} distances between the centre of potential and the centre of mass for the dark matter only simulation. With the red line, we note the 2.5σ distance from the mean of the distribution, which is our cut-off point for identifying outliers using this probe.

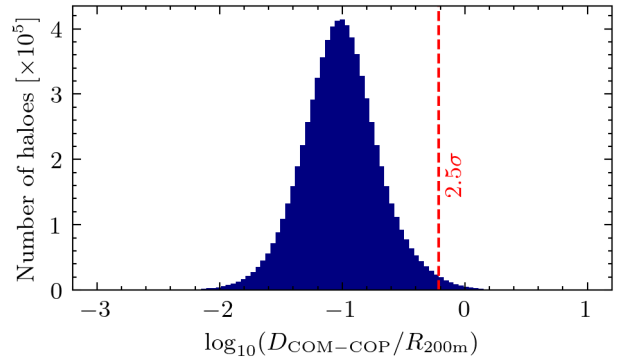


Figure 9. As in fig. 8 but for the hydro fiducial simulation.

underestimation of the mass and in this case, M_{DMO} , which according to eq. (1) will lead to high values of f_{ret} . On the other hand, outliers in the fiducial simulation will lead to low values of f_{ret} for the same reason.

We can calculate the percentage of outliers in the dark matter only simulation that also has a high value of f_{ret} as 20.05% which is an improvement over the other methods. It is also clear that most of the cases of high f_{ret} can be found in the outliers with the percentage being 50.86%. For the fiducial simulation, we want to compare it with the low values of f_{ret} . The sample however is very small so we can only calculate the percentage of haloes that have low values of f_{ret} that have been identified using the distribution for the fiducial simulation. The percentage is 85.18%, which is of course very high.

With all that in mind, we will keep this probe for future use, when we want to cut haloes that might affect our results because of issues with centre misalignment. This means that we will cut the haloes that have values of distance between the centre of potential and the centre of mass in either the dark matter only or the fiducial simulation that are 2.5σ above the mean of the corresponding distribution. We always need to be careful when we cut haloes, to not significantly bias our sample, so whenever we do that we always present the results with and without the cuts and discuss the differences.

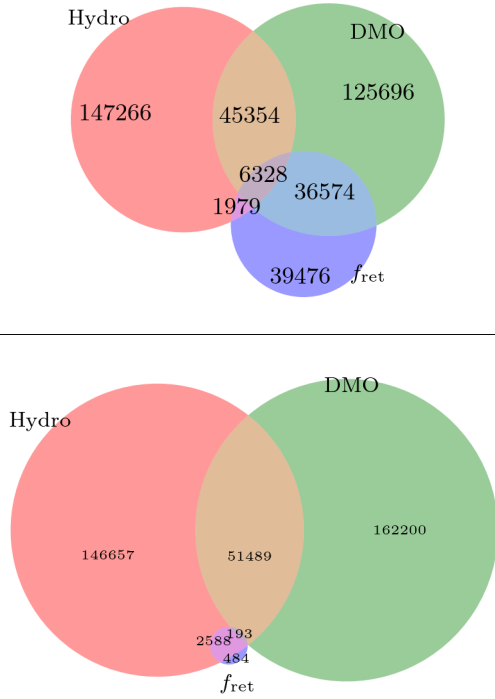


Figure 10. Venn diagrams of haloes that are identified as outliers by the distance of the centre of potential with the centre of mass of the halo for both the dark matter only simulation (DMO) and the fiducial (Hydro) simulation. To identify the outliers we take the haloes that have a distance from the mean of the distribution of more than 2.5σ . Top panel: Combined with haloes that have a value of f_{ret} that is 2σ above the average. Bottom panel: Combined with haloes that have a value of f_{ret} that is 2σ below the average.

3.2 Mass Fractions

We continue our analysis with the different mass fractions that we explore. In section 2.2 we discussed the importance of these fractions and how we can calculate them using the matching files that are present in FLAMINGO. For the ‘‘resummation’’ model, which we want to test, it is important to have accurate values for the retained mass fraction f_{ret} which is defined in eq. (1). This mass fraction, however, is artificial as it can not be reproduced in real-world observations. What we can measure is the baryon fraction f_b which is defined in eq. (2). Following the analysis in van Loon & van Daalen (2024) which is also presented in section 2.2 we can easily define the corrected baryon mass fraction f_{bc} as in eq. (4).

What we now want is to be able to connect the values of f_{bc} to those of f_{ret} as we can measure them both in our simulations. To achieve that we need to create bins of haloes, based on their mass, calculate the average of both these values and fit a relation, thus connecting f_{bc} to f_{ret} . The bins are created in a similar way as presented in section 2.4, with small modifications for this specific use. Because we want the results for different overdensity regions, we each time define the bins based on the mass of the corresponding region. We only use 8 bins, starting from $M_\Delta = 10^{12} M_\odot$, which means that we start from bin 3 in table 3. Furthermore, some of the bins in the higher mass bins, might not be populated with enough haloes to produce robust results. In those cases, we

just combine those bins that have less than 10 haloes. We also calculate the errors for f_{ret} and f_{bc} in each bin, which is the standard deviation of the mean.

To get the results we use 10 different hydrodynamical simulations and the corresponding dark matter only simulation. The first 9 are those shown in table 1, which have the same corresponding dark matter only simulation, and we also add the PLANCK simulation (which uses the PLANCK cosmology) and its corresponding dark matter only simulation, which is different from the others.

It is important that we select an appropriate fitting relation that will yield the best fitting factors. In previous work (van Loon & van Daalen 2024), a linear relation was fitted, however, with the increased grid size of FLAMINGO, which increases the sample size and reduces variance, we are able to fit a more sophisticated relation as follows:

$$f_{\text{ret}} = c - b(1 - f_{\text{bc}})^a, \quad (26)$$

where a , b , c are the three fitting parameters.

The fitting was done using the `optimize.curve_fit` function from the `scipy` module (Virtanen et al. 2020). This function uses the non-linear least-squares method to do the fitting. We are also able to use the errors on f_{ret} , which are used as weights. The function performs the fitting by minimizing the sum of the squared differences between the observed values and the values predicted by the model, with the weights as the errors:

$$\chi^2 = \sum_i \left(\frac{f_{\text{ret},i} - f_{\text{ret},i}^{\text{pred}}}{\sigma_{f_{\text{ret},i}}} \right)^2, \quad (27)$$

where $f_{\text{ret},i}$ is the observed value of f_{ret} , $f_{\text{ret},i}^{\text{pred}}$ is the predicted value of f_{ret} using the model, and $\sigma_{f_{\text{ret},i}}$ is the error on $f_{\text{ret},i}$. The sum is over all the bins. After the fitting, we can also calculate the root mean square error (RMSE) which is defined as:

$$\text{RMSE} = \sqrt{\frac{1}{N} \sum_i (f_{\text{ret},i} - f_{\text{ret},i}^{\text{pred}})^2}, \quad (28)$$

where N is the number of bins. The RMSE is a measure of the differences between the predicted values and the observed values, with a lower RMSE indicating a better fit.

Following the results and the analysis in section 3.1 we will present the results with and without excluding certain haloes that we identified as outliers using the distance of the centre of potential with the centre of mass in either the dark matter only or the hydrodynamical simulation. Those cases were excluded because they might be cases of centre misalignment, which will negatively affect our results. We expect that excluding them will drastically improve the results in the current analysis.

The results of f_{ret} as a function of f_{bc} will be shown for 7 different overdensity regions. In figs. 11 and 12 we can find the results for R_{200m} and R_{500c} . The results for the rest of the regions are included in appendix B and figs. B1 to B5.

In fig. 11 we can find the results for the R_{200m} overdensity region. On the top panel, we have the results which include all the haloes, while on the bottom panel, we have excluded the haloes we consider to be cases of centre misalignment. One first observation is that the fitting is great in both cases, always within the 1% uncertainty. The error bars for both figures are relatively small, allowing us to have great confidence that our relation is indeed correct. It is also clear that

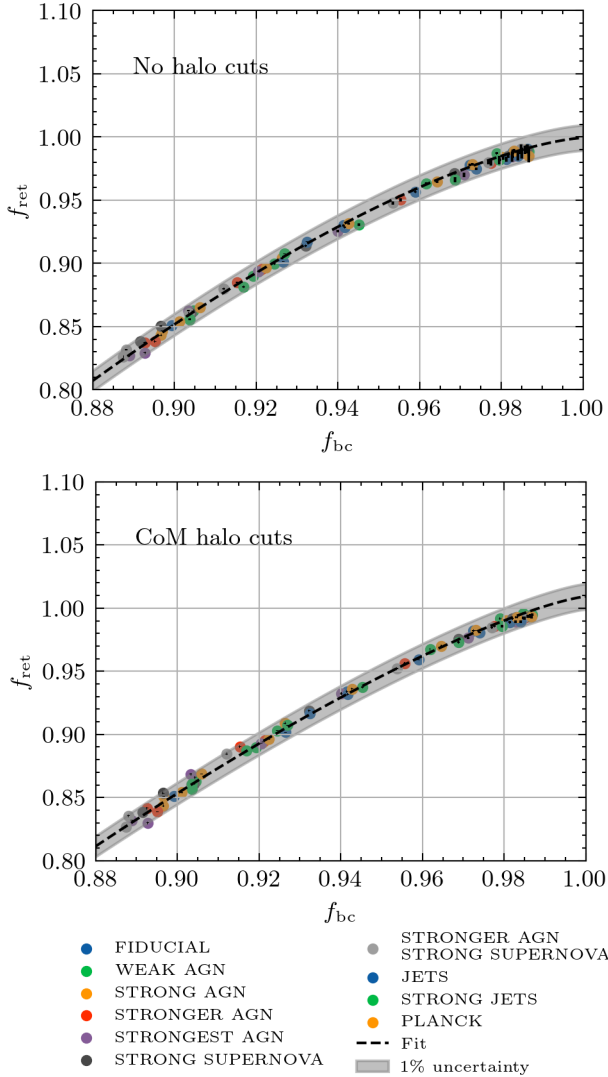


Figure 11. f_{ret} as a function of f_{bc} for the R_{200m} overdensity region. Every point on this figure represents one halo mass bin from one of the simulations. We also fit the formula shown in eq. (26). The grey area represents the 1% uncertainty. Top panel: using all haloes from the simulations. Bottom panel: excluding haloes that were identified outliers by using the distance between the centre of potential and the centre of mass. We can see that this further reduced the small errors that existed before the cuts. The fit looks good for both cases.

excluding the selected haloes has improved the errors in each bin, which points to our analysis in section 3.1 being correct. The values of the fitting parameters for all the different regions can be found in table 4 for the analysis using all the haloes and in table 5 for the analysis without the outliers.

We switch now to the R_{500c} overdensity region. The results can be found in fig. 12. This time we see that the error bars are bigger, which is expected because we are now getting results for a smaller region, near the centre of the halo, which means that the mass values are less stable and on top of that they are more sensitive to any errors in the position of the centre. We can also see that the results have highly improved when we exclude the selected haloes. On the top panel, there are many data points, especially for high f_{bc} values that are

Region	a	b	c	RMSE
R_{50c}	1.45	4.05	1.00	0.003
R_{200m}	1.45	4.15	1.00	0.003
R_{100c}	1.49	4.70	1.00	0.004
R_{200c}	1.58	5.91	1.00	0.005
R_{500c}	1.78	9.71	1.00	0.011
R_{1000c}	1.88	12.98	1.01	0.025
R_{2500c}	2.74	94.96	1.01	0.018

Table 4. The fitting parameters for f_{ret} as a function of f_{bc} following eq. (26) for the different overdensity regions, with all the haloes (no halo cuts). We also include the RMSE to measure the goodness of fit. We notice that the RMSEs for the smaller regions are significantly smaller.

Region	a	b	c	RMSE
R_{50c}	1.31	3.11	1.01	0.003
R_{200m}	1.31	3.16	1.01	0.003
R_{100c}	1.31	3.30	1.01	0.005
R_{200c}	1.37	3.98	1.02	0.006
R_{500c}	1.42	4.77	1.03	0.008
R_{1000c}	1.59	6.92	1.03	0.016
R_{2500c}	2.37	41.14	1.02	0.017

Table 5. As in table 4 but with the cuts for the distance between the centre of potential and the centre of mass. We notice that RMSEs have improved for the larger regions. The parameters of a and b for the small regions have also notably changed.

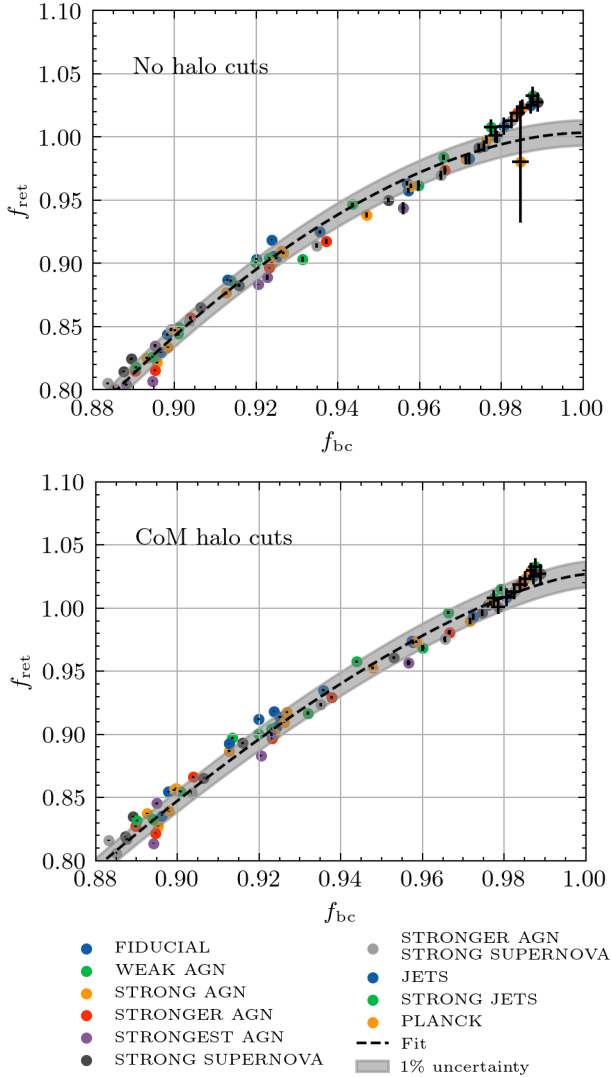
clearly outside the 1% uncertainty region. This picture is different in the bottom panel, where the number of points outside that region has reduced, and so has the distance of the points from the fitting line. Note that the fitting is redone in each panel. For the RMSEs, we can once again look at tables 4 and 5.

It is interesting to also note how the fitting parameters have changed for the small regions. In those regions, the fitting is very accurate in both cases (with and without the cuts) with small values for the RMSE. However, it is noticeable that the value of parameter a , which is the exponent in eq. (26), has changed from 1.45 (for R_{50c} and R_{200m}) to 1.31. Since there are no significant changes in the error bars between the two cases (cuts or not cuts), this can be evidence of biasing.

If we look closer at the two panels of fig. 11 we can see that most of the points are now higher on the y-axis (f_{ret} , while they remain in the same position on the x-axis (f_{bc}). This is an indication of biasing towards higher f_{ret} , by cutting proportionally more low values.

One other interesting thing to note is how tightly all simulations follow the relation between f_{ret} and f_{bc} . From the analysis in section 2.2, this is something that we expected since if dark matter did not respond to the changes of the halo due to baryonic feedback we would have an exact match between the two values ($f_{\text{ret}} = f_{\text{bc}}$). This means that the relation between the two should only depend on how much baryonic mass was removed from the halo, and not on the mechanism of removal. This means that despite different simulations causing different proportions of baryonic mass to be removed from the haloes, the retained mass will always be proportional to the value of f_{bc} .

Following the analysis of the results that have been presented in this section, we will keep the fitting results of both



cases, with and without the halo cuts. When applying the model we will compare the two results to see if it improves the performance of the model and if there are indications of biasing the sample, which is something we must be aware of.

3.3 Power Spectra

The power spectrum is a great tool to study the distribution of matter and an important component of our model. In this section, we will apply the methods we discussed in section 2.5 and analyse the results.

3.3.1 Auto Power

The matter-matter auto-power spectrum is the spectrum of all the matter of the full simulation with itself. Some of these calculations have already been performed in FLAMINGO using the SWIFT code. For our purposes, we use the results for the

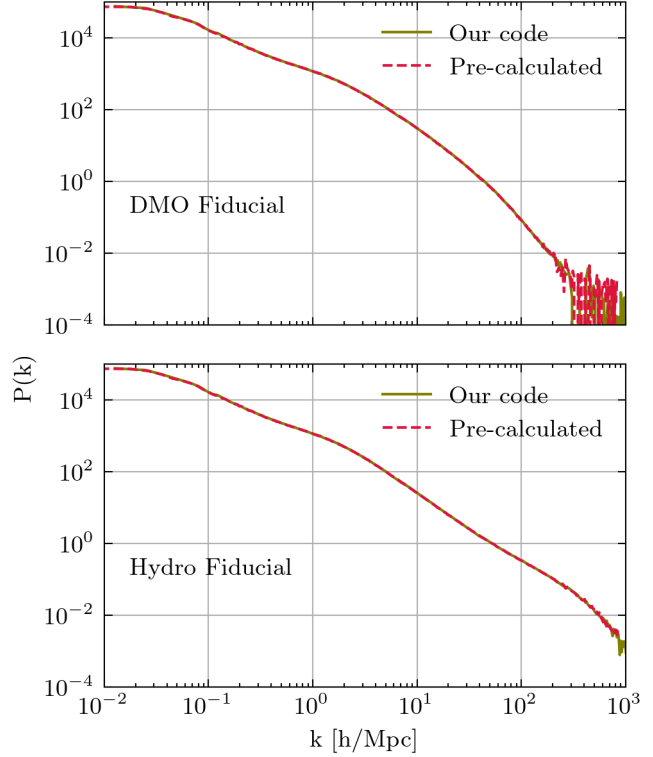


Figure 13. The matter-matter auto-power spectrum for the dark matter only simulation (top panel) and the hydro fiducial (bottom panel). With red, we have the pre-calculated spectrum from FLAMINGO, while with green is the spectrum that was calculated using our code. We see that our calculations precisely match the pre-calculated spectrum.

dark matter only and hydro fiducial simulation, to make sure that our code performs as expected.

In fig. 13 we can see the results for the dark matter only (top panel) and the hydro fiducial (bottom panel) simulation. With the red line, we have the spectrum as it was calculated in FLAMINGO and with a green line we have our own implementation of the auto-power spectrum. We can see that the agreement between the two is very precise on all scales, even the ones that would be dominated by the shot noise, which we have subtracted (as it was also already done in the FLAMINGO spectrum). The resolution of the simulation allows us to go to values of k higher than $100 h/\text{Mpc}$. For the hydro simulation, because of the increased number of particles and the fact that particles will cluster more on small scales, we are able to go as high as $k = 1000 h/\text{Mpc}$.

3.3.2 Cross Power

The matter-halo cross-power spectrum is the power spectrum of the matter of a halo (or group of haloes) with the matter of the whole simulation. For this analysis, we are mainly interested in the dark matter only simulation, as our model (described in section 2.6) uses that as an input. One very important consideration, that will also play a role when applied to our model is the region we use to define the haloes. We have obtained results for all 7 different overdensity regions that have been used throughout the current work.

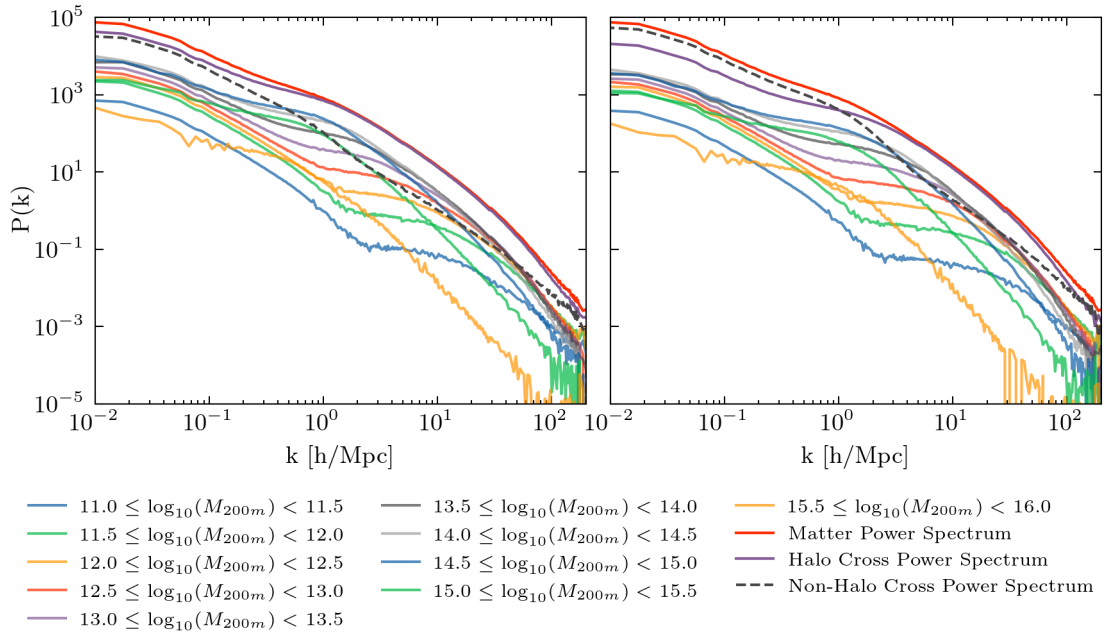


Figure 14. The matter-halo cross-power spectrum for all the different bins for the dark matter only simulation. We also plot the matter-matter auto-power spectrum and the total halo cross-power spectrum, which is the sum of all the cross-power components from the different bins. The non-halo cross-power spectrum is calculated by subtracting the total halo cross-power from the auto-power spectrum. Left panel: we define the haloes using the R_{200m} . Right panel: we define the haloes using the R_{500c} .

In fig. 14 we show the results when using the R_{200m} (left panel) and R_{500c} (right panel) regions to define the haloes. The plots show the cross-power spectra of all the different bins as we discussed in section 2.4. The matter-matter auto-power spectrum for the dark matter only simulation is also shown in the plot. One can consider the different contributions to the total matter power spectrum. First, we have all the different halo components, which are the different bins we use in this analysis. This is the matter that is highly clustered in small regions and is expected to dominate, especially in high values of k . We calculate the total of this contribution by summing the cross-power spectra of all the different bins. Finally, we also have the contribution from matter that is not part of the haloes. This mass is not highly clustered (although some clustering is expected, especially around the haloes) and, therefore, we expect it to not be a dominant contribution on smaller scales.

The results of fig. 14 confirm this hypothesis. If we look at the results for the region R_{200m} we can see that on small scales (high k) we have a complete domination of the halo cross-power contribution. On very large scales the halo and non-halo contribution is around equal. When we define the haloes using the R_{500c} region, which is significantly smaller than the R_{200m} region, we can still see similar results. The main difference is that we now have less mass in our haloes which drops the significance of the cross-power contribution and the non-halo spectrum now dominates for significantly higher k than before. Still, on small scales, we return to a halo cross-power domination of the total matter power spectrum.

We have performed the same calculations for all 7 over-density regions we have discussed so far (R_{50c} , R_{200m} , R_{100c} , R_{200c} , R_{500c} , R_{1000c} , R_{2500c}). The results for the 5 regions not shown here are very similar to the ones in fig. 14. Al-

though we chose not to show them, we will use those results in the next section where we will apply the model for all the different regions.

3.4 “Resummation” Model

The final piece of our analysis is of course to apply the “resummation” model as described in section 2.6. As we have already mentioned in that section, we explore two ways of using the model; one is by using only one set of cross-power spectra (we will refer to this as the model for “one region”), and the other is to use two sets with different regions being used for the definition of the haloes (we will refer to this as the model for a “combination of two regions”).

Following the discussion on the results for the f_{ret} as a function of f_{bc} (section 3.2) we will show the results using the fitting results for both cases; with and without the cuts for the centre of mass outliers. It is important to also note that for the model we always use all the haloes, without any cuts, regardless of which fitting results we use for f_{ret} . We essentially only use the cuts to obtain a better fit but then apply it to all the haloes. The drawback of doing this is that the sample of haloes with the cuts is biased compared with the full sample that we use for the model. This can cause issues for the model if the biased sample is not able to generalize well. On the other hand, the increased accuracy of the fitting parameters can lead to better model results. For all of that, it is important that we compare both results before drawing some conclusions.

3.4.1 One Region

In this part, we will discuss the results of the “resummation” model using one set of cross-power spectra. In theory, we can use any of the results mentioned in section 3.3.2, each will give slightly different results, with better or worse match with the true power suppression. As we have already discussed, to study the power suppression we need the matter-matter auto-power spectra from a hydro simulation and the corresponding dark matter only simulation. If we have that the power suppression is simply:

$$\frac{P_{\text{hydro}}}{P_{\text{DMO}}}(k), \quad (29)$$

where P_{hydro} and P_{DMO} are the auto-power spectra for the hydro and dark matter only simulations respectively, which are both dependent on the wavenumber k .

We can use our model as described in section 2.6 to basically model the auto-power of the hydro simulation. By doing that we can get the expected power suppression by only using the dark matter only simulation. It is important to note that we also need the retained mass ratio f_{ret} , which we can get using the corrected baryonic fraction (f_{bc}) and the fitting results we discussed in section 3.2. Following the discussion on that section we have two fitting results, one by using the halo cuts we investigated in section 3.1 and one without any halo cuts. For this part, we will show both results and compare them. We will start with the results that are based on the fits with the halo cuts and then move to the ones without.

In fig. 15 we have our first model results. The three panels show from top to bottom the results for the R_{200m} , R_{200c} and R_{500c} regions. The figure includes the true power suppression as well as the confidence intervals of 1, 2 and 5 % to help us judge how well our model performs. For the R_{200m} region we can see that the model performs relatively well for the large scales, and is within the 1% limit for $k < 2 h/\text{Mpc}$. However, it fails to produce a good match for the small scales. This is something that we expect as the R_{200m} region is relatively large, and thus, doesn’t enable us to get a good precision for the mass loss in the small regions.

We continue with the results for the R_{200c} region, which are shown in the middle panel of fig. 15. This region is now smaller than R_{200m} which should allow us to model the power suppression better on smaller scales. As we can see from the figure this is indeed the case, as the model is always within 5% of the true power suppression, even for large values of k . We can notice, however, that the fit for the large scales has gotten a bit worse, compared with the top panel.

The final region we show in this section is the R_{500c} , which is smaller than both the R_{200m} and R_{200c} regions. The model results for this region are shown in the bottom panel of fig. 15. We can see that the model is now within 2% of the true power suppression on almost all values of k which is a notable improvement from the results for R_{200c} . Compared with the results for R_{200m} , the large scales are a bit worse, however, the small scale results are now far superior. This is something that we were expecting since as we already mentioned, using smaller regions can help model the loss of mass for smaller scales.

We will now switch to the model results using the fitting results without any cuts. These results are shown in fig. 16 for the R_{200m} , R_{200c} and R_{500c} regions (top, middle and bottom panels respectively). We want to compare them with the

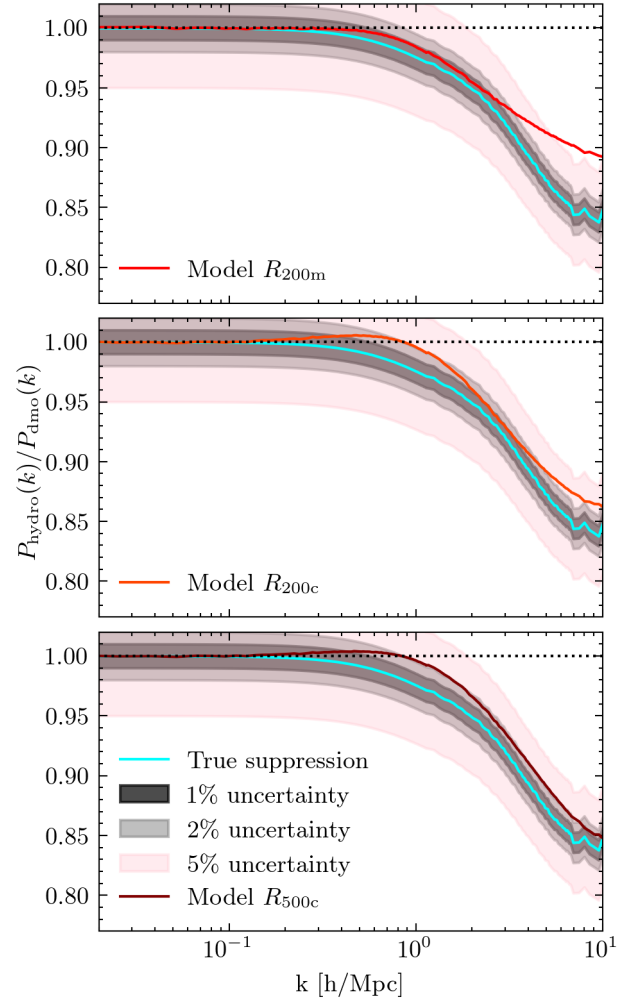


Figure 15. Model results for the hydro fiducial simulation using the fitting results with the halo cuts. Top panel: for the R_{200m} region, middle panel: for the R_{200c} region, bottom panel: for the R_{500c} region. The blue line shows the true power suppression with the 1, 2 and 5 % uncertainty. With the red line, we show the modelled power suppression. We can see that by using the R_{200m} region we can model well the power suppression on large scales, with the R_{200c} region the scales around 2 to 3 h/Mpc , and with the R_{500c} region the small scales.

corresponding figures for the previous results, where we were using the halo cuts. We can see that they all show a slight but noticeable improvement, especially in the areas we expect to have a good fit. For the R_{200m} (top panel in both figs. 15 and 16) we see an improvement on large scales. The same is true for R_{200c} (middle panels) and R_{500c} (bottom panels) for the small scales.

With this analysis, we can say that the halo cuts we discussed in section 3.1 do not improve the model results for one region, on the contrary, they make them slightly worse. This could mean that we have some level of bias that we introduced when applying the halo cuts (for f_{ret} but not for the cross-power spectra), which leads to these results. We will of course keep using both of them when applying the model for two regions to make our final assessment of which one has a better accuracy.

We have also applied the model for all the other hydro

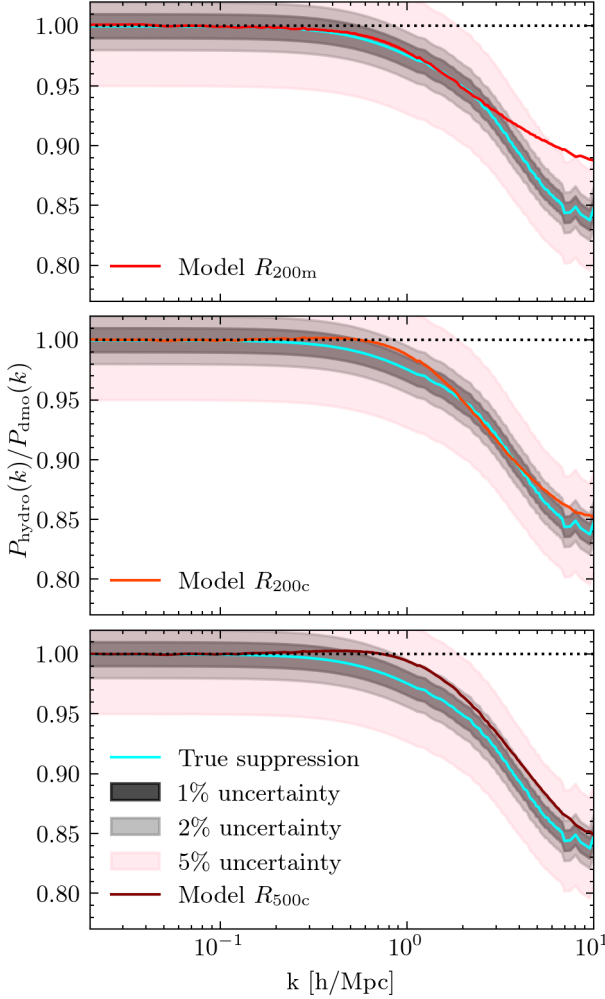


Figure 16. As in fig. 15 but this time using the fitting results with no cuts. We can see an improvement in fit in all three panels, compared with the model results using the fitting results with the cuts.

simulations and for all the 7 different regions we have used so far. Some of those results are shown in appendix C with the halo cuts and in appendix D without any cuts.

3.4.2 Combination of two Regions

In addition to the models where we use one set of cross-power results for one region, we can also apply the model using two sets that use a different region for the definition of haloes. As we have already discussed, large regions are better suited to describe power suppression on large scales. On the other hand, smaller regions are better equipped to measure the mass loss near the centre of the halo, and thus provide a better probe for power suppression on small scales. It, therefore, makes sense to combine one large and one small region, getting the best of both cases. In this section, we will analyze all 3 possible combinations of the 3 regions we have shown in section 3.4.1 (R_{200m} , R_{200c} , R_{500c}). We will keep using the fiducial simulation to compare the different results.

We start fig. 17 where we see the model results when we use the fitting with the halo cuts. From top to bottom, we

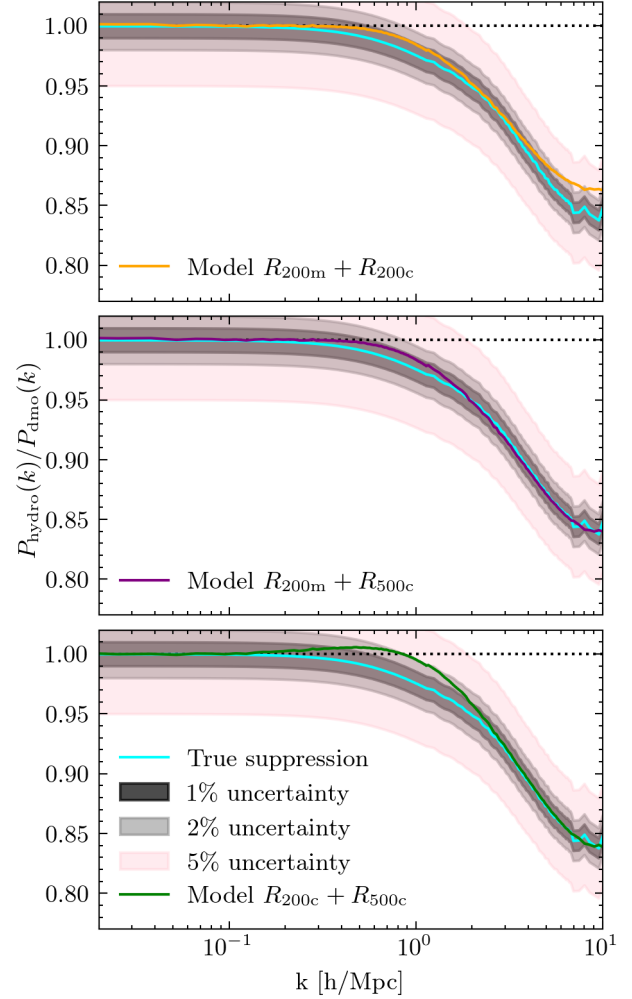


Figure 17. Model results for the hydro fiducial simulation, using a combination of 2 regions. Top panel: using the R_{200m} and R_{200c} regions, middle panel: using the R_{200m} and R_{500c} regions, bottom panel: using the R_{200c} and R_{500c} regions. For these results, we use the fitting results with the halo cuts. The blue line shows the true power suppression with the 1, 2 and 5 % uncertainty. With the purple line, we show the modelled power suppression. In all three results, we see a great improvement over the model results using one region. The combination of the R_{200m} and R_{500c} regions (middle panel) show the best fit across all scales.

have the results for the combination of R_{200m} and R_{200c} , the combination of R_{200m} and R_{500c} and the combination of R_{200c} and R_{500c} . For all of these models, we can see an improved accuracy over any of the models using only one region. For the top panel, we can clearly see the influence of each individual region we use. The shape of the model for large scales very closely resembles the results we got when we were only using the R_{200m} region (top panel of fig. 15), while on the smaller scales, it is almost the same as in the results we got for the region R_{200c} (middle panel of fig. 15). This is something that we expected since we use the smaller region to probe the mass loss near the centre of the halo and the large region for the outskirts of the halo.

In the middle panel of fig. 17 we have the results for the combination of R_{200m} with R_{500c} . These are the two extremes out of the three regions we discussed so far, and as we can see

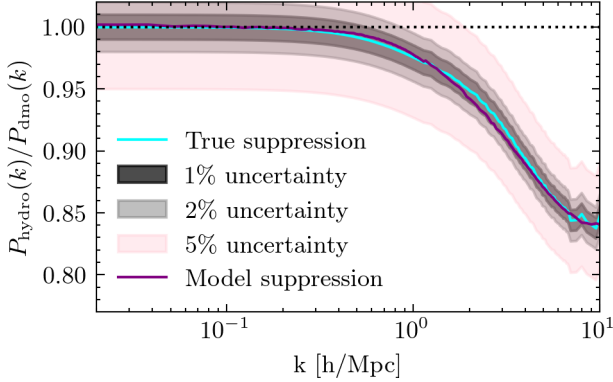


Figure 18. Model result for the hydro fiducial simulation, using the combination of R_{200m} and R_{500c} . For this result, we use the fitting results without any halo cuts. The blue line shows the true power suppression with the 1, 2 and 5 % uncertainty. With the purple line, we show the modelled power suppression. We see that the fit is clearly worse than the results with halo cuts, especially for small scales.

the results show the best match to the true power suppression. When we compare it with the top panel, where we use the R_{200c} region for the small scales, it becomes clear that the R_{500c} region allows us to better follow the mass loss near the centre than the R_{200c} region which is relatively larger.

Finally, we have the results for the combination of R_{200c} and R_{500c} , which are shown in the bottom panel of fig. 17. We see that the fitting is great for the high values of k , which is something we expected since it must be very similar to the middle panel since both use the same small region (R_{500c}). However, for the small k values, the model is no longer within 1% of the true power suppression. The reason is that the R_{200c} region is not large enough to give great results for the large scales.

From the previous analysis, we can clearly say that the model that best matches the power suppression for all the different scales in the hydro fiducial simulation is the one that uses the combination of R_{200m} and R_{500c} . We can now compare this and see if using the fitting results for f_{ret} without the halo cuts will improve the model or not. In fig. 18 we have the results for the same two regions but without the halo cuts. We see that in contrast to the results we got for the one region model (section 3.4.1), this time the results are worse than when we include the halo cuts. It is also interesting to note that the model overpredicts the degree of power suppression, contrary to any other model result, which always underpredicts relative to the true power suppression. This overestimation of the power suppression on small scales leads to an overall worse match with the true power suppression. For the large scales, there is a slight improvement, it is however not sufficient for us to consider this result as better than the previous one. Although not shown here, this also extends to the other simulations we have used throughout this work.

One possible explanation for this behaviour is that we indeed have some biasing when we remove the haloes for the f_{ret} fitting. We, however, compensate for that by highly improving the fit in the small regions (like R_{500c}), which without the halo cuts suffered from high error bars and a poor fit. We will discuss this further in section 4. For now, we will con-

tinue with the model results that gave us the best match to the true power suppression, and that is the combination of R_{200m} with R_{500c} , including the halo cuts.

For the final result, we have a collective plot of the model with the true power suppression for all 9 hydro simulations we used in this work, split over the two panels of fig. 19. For all the different simulations we still use the same relations for f_{ret} and f_{bc} , only changing the f_{bc} values, which we calculate using the haloes of each simulation. We can see that our model with the best regions greatly matches the true power suppression over all scales and different degrees of baryonic feedback. On the left panel, we have the AGN as the mechanism of baryonic feedback for different intensities. The suppression is larger for the higher intensities, our model can however give great predictions even on small scales, almost always within 1% of the true values. The only exception in this is the very small scales ($k > 4 h/\text{Mpc}$) for the strongest AGN simulation, but even in this case the model remains at least within the 2% region of the true power suppression.

On the right panel of fig. 19, we have some different mechanisms, supernovae and jets, which our model can also describe the power suppression they produce with high accuracy. For the simulations using jets (jets and strong jets), we see that the model is not within the 1% accuracy. Especially for the strong jets, on large scales, the model is well outside the 1% region. As we have already discussed, the jets use also an AGN feedback mechanism, but instead of using thermal AGN, they use AGN jets. This mechanism distributes the mass non-uniformly around the haloes, which can cause some different clustering to appear outside of them, which is different from the way matter usually clusters outside the haloes. Since our model uses the way the matter was clustered outside the dark matter only haloes, to model the clustering of mass removed from them, it is unable to take into consideration some different ways of clustering. Jets are also able to eject matter to greater distances than the thermal AGN process. This means that we need bigger regions to better probe the matter distribution on a large scale. However, applying the model using the R_{50c} region in combination with others did not improve the results compared with R_{200m} . In appendices C and D we show the one region models for this simulation using the R_{50c} and R_{200m} regions.

From this analysis, we can say that the “resummation” model was able to match the power suppression in all of the hydro simulations from the FLAMINGO suite we have used. When we use the appropriate regions (R_{200m} and R_{500c}) it produces results that match the true values within 1% with the exception of the two simulations using jets. The implications of these results will be discussed in the next section.

4 CONCLUSIONS

In this section, we will further discuss the results we analyzed in section 3 and their implications. We will also propose future steps for this work.

We have extensively discussed the issue of centre misalignment in FLAMINGO. In section 3.1 we have explored two different probes to detect such cases. The first one was the mass profiles of the haloes. This method uses the general intuition that the mass profile of a halo with a wrongly positioned centre should be different from the general trend of mass profiles.

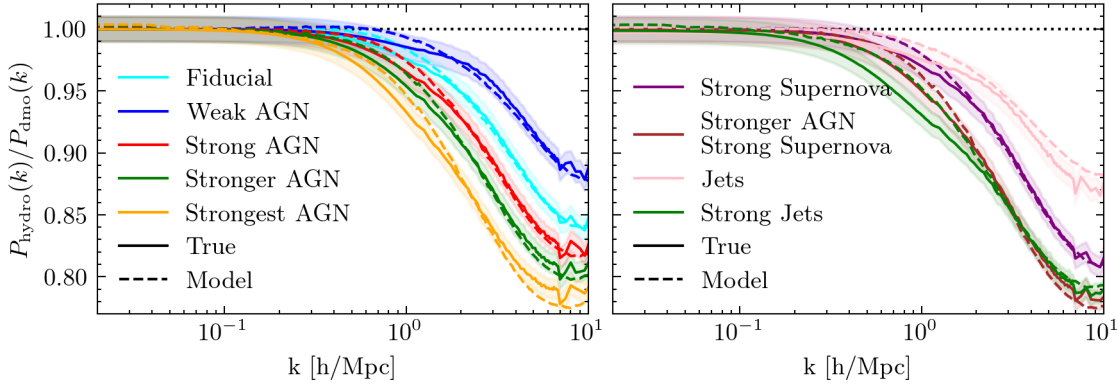


Figure 19. Collective plot of the model results for all 9 different simulations we used in this work. The model uses the combination of R_{200m} and R_{500c} , which has shown the best match to the true suppression. The true power suppression is represented each time with a solid line, while the model is denoted with a dashed line. We also include the areas of 1% uncertainty for each simulation. Left panel: the fiducial, weak AGN, strong AGN, stronger AGN and strongest AGN simulations. Right panel: the strong supernova, strong AGN strong supernova, jets and strong jets simulations. In general, we see a great fit for all the simulations.

The reason for that is that smaller regions are expected to be denser than larger ones (if the centre is correct). If the centre is misaligned, it will usually be in a less dense location resulting in a profile with less mass for small regions (compared with a typical profile) and a faster accumulation of mass in larger regions. While our results have shown some promising signs (see section 3.1.1 and also appendix A) we were not able to use this probe for detecting many cases of centre misalignment without also catching many haloes with correct centres. We also attempted to combine this probe with the normalized distance between the centres of the potential of the dark matter only and hydro simulations, with no improvement over the results.

The second probe that was used, was the normalized distance between the centre of potential and the centre of mass. This probe proved to be far more reliable (see section 3.1.2) and we were able to get a significant number of haloes with wrong centres by cutting out the haloes that had a distance between the two centres 2.5σ above the mean distance. The results for all of the probes were always compared with the outliers in the values of f_{ret} , which we have shown (section 2.3) to be very sensitive to wrong positions for the centre of the haloes, but can not be directly used to eliminate such cases because it will highly bias the sample.

We have also performed a detailed mapping between the values of f_{ret} and f_{bc} . This is a crucial step for our model as being able to obtain accurate values for f_{ret} will greatly impact its final performance. For the fitting, we binned the haloes of each simulation based on their mass and calculated the average values for f_{ret} and f_{bc} with the appropriate errors. We performed the fitting independently for each of the 7 overdensity regions we used to define our haloes. Results have shown to be stable for large regions with no significant change for the fitting parameters for regions larger than the R_{100c} region. The RMSEs were also significantly lower for those regions, which is something we expected since larger regions are less prone to errors that can come from random noise or systematics (like centre misalignment). We also performed independent fitting for a sample of haloes where we excluded the haloes that we previously defined as outliers based on their distance between the centre of mass and the

centre of potential. These fitting results showed an improved RMSE for smaller regions (R_{500c} and R_{1000c}) but not for the smallest region (R_{2500c}) where other sources of error are more significant. For the larger regions there was no improvement in the RMSE, we noticed, however, a change in the values of the fitting parameters which as we mentioned are stable for each of the two samples.

For the calculation of power spectra, we have developed a PYTHON script to make the process more efficient. The script utilizes a technique of folding the real space which is described more extensively in section 2.5. The results in section 3.3 confirm that the code was implemented correctly by comparing the auto-power spectra with the ones calculated using SWIFT. We then proceed to calculate the cross-power spectra for all the binned haloes in the dark matter only simulation and for all the different regions we use to define the haloes. From that, we can calculate the total halo cross-power spectrum and subtract it from the auto-power spectrum to obtain the non-halo cross-power spectrum.

The power spectra we have calculated are used to apply the ‘‘resummation’’ model which was introduced in van Loon & van Daalen (2024) and described in section 2.6. For the model, we also use the fitting results for f_{ret} , with and without the halo cuts as we have previously mentioned. We have applied the model using only one region and also for two regions. The results for two regions show a big improvement over those with one region, which is something we expected, as the two regions allow us to probe better the large and small scales at the same time, by choosing the appropriate regions. Interestingly, for the results with one region, we observed that the halo cuts in the f_{ret} fitting have decreased the accuracy of the model. The reason behind that is probably the biasing of the sample when removing certain haloes. Further exploration on this topic is still needed, as to what caused this biasing, if, for example, we removed a proportionally larger percentage of massive haloes. Nevertheless, this biasing did not highly affect the results we got for the model using two regions. In this case, the results using the f_{ret} fitting with the halo cuts show an improvement over the ones with no halo cuts. The improved fitting accuracy for the small regions probably played a more crucial role in this case as it

allowed us to, more carefully, probe the power suppression in the small scales.

In total, we used 9 different hydro simulations in our analysis. The simulations we used varied the intensity of different baryonic feedback mechanisms. The fiducial simulation is used as the basis from which we can compare all the others. For all of them, we find that our model performs relatively well. With the exception of the two simulations using jets and the very small scales of the strongest AGN simulation, we find that all the other models are able to be within the 1% accuracy region of the true power suppression. For the two simulations using jets, we see that our model had its worst performance. For the jets simulation, we notice a mismatch in the very small scales ($k > 4 h/\text{Mpc}$), similar to what we got for the strongest AGN simulation, and also on the large scales. For the strongest jets, the mismatch in the large scales is even more pronounced, although the performance in small scales is almost perfect. The reason behind this inaccuracy of the model in these particular simulations has to do with the physics of the mechanism itself. These simulations use AGN jets instead of thermal AGNs which are used in all other simulations. Jets are known to distribute mass in a non-uniform way and also expel mass at greater distances than all the other mechanisms. Our model uses different regions to probe different scales, however, none of the available overdensity regions is sufficient in this case (also see appendices C and D). Additionally, our model assumes that matter ejected from the haloes will cluster like the matter that was already there. Any deviation from that will also cause accuracy issues. Further exploration for these simulations needs to be done, by also looking at simulation sets with higher resolution and/or bigger box size.

To summarize the whole process, we were able to successfully apply the “resummation” model from [van Loon & van Daalen \(2024\)](#) to the **FLAMINGO** suite of simulations. To achieve that we had to get the cross-spectra for the binned haloes and the auto-power spectrum for the dark matter only simulation. Then, to properly rescale the spectra we had to map f_{ret} to f_{bc} , using bins of haloes. During this process, we also had to deal with the misalignment issues of the halo centres in **FLAMINGO**.

Future research will study if the model can be successfully applied to different snapshots for higher values of redshift. So far we have only used the snapshot that corresponds to $z = 0$. We are also interested in testing the model for simulation sets that use a bigger box size or a higher resolution. Using higher resolutions could allow us to better map f_{ret} with f_{bc} for the smaller regions (R_{1000c} and R_{2500c}). For the simulation set we have used, because of the big fitting errors for these regions, we were unable to properly use them for the model, but if this changes for a higher resolution, as we assume, then we should be able to have accurate results with our model for even smaller scales. The simulations with bigger box sizes will increase the sample size and reduce the variance, which should also improve the fitting results.

It is also worth exploring the issue of centre misalignment in the **FLAMINGO** simulations and how it affects the mapping between f_{ret} and f_{bc} . We have shown how by using the distance between the centre of potential and the centre of mass for each halo, we can identify many cases of centre misalignment, but this comes at the cost of biasing the sample of haloes we use. Fixing the issue of centre misalignment will

be the ideal solution for this case, and there is an active try to understand the reasons behind it and how to properly address them. For our purposes, however, examining more clever and efficient ways to identify haloes with wrong centres, will greatly improve the fitting parameters between f_{ret} and f_{bc} and as a result the final accuracy of the model.

As a final note, the code we have developed for analyzing the simulations and getting the power spectra can be utilized in many other projects, especially for the **FLAMINGO** simulations. For more information on that, please contact any of the authors.

ACKNOWLEDGEMENTS

I would like to personally thank my supervisor, Marcel van Daalen, for our collaboration in this project. His guidance greatly helped me in many different aspects of this work, and I greatly enjoyed all our conversations, technical or not. I also want to thank him for the trust he showed to me in this whole process. I also want to thank Jim, Levi and Rutger, all of whom worked on different projects on the **FLAMINGO** simulations. The “FLAMINGO group” as I like to call it, made this year-long project more fun. Finally, I want to thank my family, friends and my girlfriend Polina for the love and support they showed to me in this endeavour.

REFERENCES

- Abbott T. M. C., et al., 2022, *Phys. Rev. D*, **105**, 023520
- Abdalla E., et al., 2022, *Journal of High Energy Astrophysics*, **34**, 49
- Angulo R. E., Hahn O., 2022, *Living Reviews in Computational Astrophysics*, **8**, 1
- Aricò G., Angulo R. E., Hernández-Monteagudo C., Contreras S., Zennaro M., Pellejero-Ibañez M., Rosas-Guevara Y., 2020, *MNRAS*, **495**, 4800
- Aricò G., Angulo R. E., Hernández-Monteagudo C., Contreras S., Zennaro M., 2021, *MNRAS*, **503**, 3596
- Bartelmann M., Schneider P., 2001, *Phys. Rep.*, **340**, 291
- Bond J. R., Cole S., Efstathiou G., Kaiser N., 1991, *ApJ*, **379**, 440
- Borrow J., Borrisov A., 2020, *The Journal of Open Source Software*, **5**, 2430
- Borrow J., Kelly A. J., 2021, *arXiv e-prints*, p. arXiv:2106.05281
- Chisari N. E., et al., 2019, *The Open Journal of Astrophysics*, **2**, 4
- Coil A. L., 2013, in Oswalt T. D., Keel W. C., eds., , Vol. 6, *Planets, Stars and Stellar Systems. Volume 6: Extragalactic Astronomy and Cosmology*. Springer Netherlands, p. 387, doi:10.1007/978-94-007-5609-0_8
- Cooley J. W., Lewis P. A. W., Welch P. D., 1969, *IEEE Transactions on Education*, **12**, 27
- Cooray A., Sheth R., 2002a, *Phys. Rep.*, **372**, 1
- Cooray A., Sheth R., 2002b, *Phys. Rep.*, **372**, 1
- Debackere S. N. B., Schaye J., Hoekstra H., 2020, *MNRAS*, **492**, 2285
- Duffy A. R., Schaye J., Kay S. T., Dalla Vecchia C., 2008, *MNRAS*, **390**, L64
- Duffy A. R., Schaye J., Kay S. T., Dalla Vecchia C., Battye R. A., Booth C. M., 2010, *MNRAS*, **405**, 2161
- Elahi P. J., Cañas R., Poulton R. J. J., Tobar R. J., Willis J. S., Lagos C. d. P., Power C., Robotham A. S. G., 2019, *Publ. Astron. Soc. Australia*, **36**, e021
- Euclid Collaboration et al., 2019, *MNRAS*, **484**, 5509
- Euclid Collaboration et al., 2021, *MNRAS*, **505**, 2840
- Euclid Collaboration et al., 2024, *A&A*, **684**, A138

- Gao L., Theuns T., 2007, *Science*, **317**, 1527
- Gavazzi R., Treu T., Rhodes J. D., Koopmans L. V. E., Bolton A. S., Burles S., Massey R. J., Moustakas L. A., 2007, *ApJ*, **667**, 176
- Giocoli C., Bartelmann M., Sheth R. K., Cacciato M., 2010, *MNRAS*, **408**, 300
- Hand N., Feng Y., Beutler F., Li Y., Modi C., Seljak U., Slepian Z., 2018, *AJ*, **156**, 160
- Hearin A. P., Zentner A. R., Ma Z., 2012, *J. Cosmology Astropart. Phys.*, **2012**, 034
- Hoekstra H., Hsieh B. C., Yee H. K. C., Lin H., Gladders M. D., 2005, *ApJ*, **635**, 73
- Huterer D., Takada M., 2005, *Astroparticle Physics*, **23**, 369
- Jenkins A., et al., 1998, *ApJ*, **499**, 20
- Jing Y. P., Zhang P., Lin W. P., Gao L., Springel V., 2006, *ApJ*, **640**, L119
- Joachimi B., Bridle S. L., 2010, *A&A*, **523**, A1
- Kilbinger M., 2015, *Reports on Progress in Physics*, **78**, 086901
- Kugel R., et al., 2023, *MNRAS*, **526**, 6103
- Laureijs R., 2009, *arXiv e-prints*, p. arXiv:0912.0914
- Laureijs R., et al., 2011, *arXiv e-prints*, p. arXiv:1110.3193
- Le Brun A. M. C., McCarthy I. G., Schaye J., Ponman T. J., 2014, *MNRAS*, **441**, 1270
- Liu G., Wang Y., Zhao W., 2024, *Physics Letters B*, **854**, 138717
- Mandelbaum R., Seljak U., Kauffmann G., Hirata C. M., Brinkmann J., 2006, *MNRAS*, **368**, 715
- McCarthy I. G., Schaye J., Bird S., Le Brun A. M. C., 2017, *MNRAS*, **465**, 2936
- McKerns M. M., Strand L., Sullivan T., Fang A., Aivazis M. A. G., 2012, *arXiv e-prints*, p. arXiv:1202.1056
- Mead A. J., Peacock J. A., Heymans C., Joudaki S., Heavens A. F., 2015, *MNRAS*, **454**, 1958
- Mead A. J., Brieden S., Tröster T., Heymans C., 2021, *MNRAS*, **502**, 1401
- Peacock J. A., Smith R. E., 2000, *MNRAS*, **318**, 1144
- Press W. H., Schechter P., 1974, *ApJ*, **187**, 425
- Rudd D. H., Zentner A. R., Kravtsov A. V., 2008, *ApJ*, **672**, 19
- Salcido J., McCarthy I. G., Kwan J., Upadhye A., Font A. S., 2023, *MNRAS*, **523**, 2247
- Schaller M., et al., 2024, *MNRAS*,
- Schaye J., et al., 2010, *MNRAS*, **402**, 1536
- Schaye J., et al., 2015, *MNRAS*, **446**, 521
- Schaye J., et al., 2023, *MNRAS*, **526**, 4978
- Schneider A., Teyssier R., 2015, *J. Cosmology Astropart. Phys.*, **2015**, 049
- Schneider A., et al., 2016, *J. Cosmology Astropart. Phys.*, **2016**, 047
- Schneider A., Teyssier R., Stadel J., Chisari N. E., Le Brun A. M. C., Amara A., Refregier A., 2019, *J. Cosmology Astropart. Phys.*, **2019**, 020
- Schneider A., Stoira N., Refregier A., Weiss A. J., Knabenhans M., Stadel J., Teyssier R., 2020a, *J. Cosmology Astropart. Phys.*, **2020**, 019
- Schneider A., et al., 2020b, *J. Cosmology Astropart. Phys.*, **2020**, 020
- Seljak U., 2000, *MNRAS*, **318**, 203
- Semboloni E., Hoekstra H., Schaye J., van Daalen M. P., McCarthy I. G., 2011, *MNRAS*, **417**, 2020
- Semboloni E., Hoekstra H., Schaye J., 2013, *MNRAS*, **434**, 148
- Spergel D. N., et al., 2007, *ApJS*, **170**, 377
- Springel V., Frenk C. S., White S. D. M., 2006, *Nature*, **440**, 1137
- Tinker J., Kravtsov A. V., Klypin A., Abazajian K., Warren M.,Yepes G., Gottlöber S., Holz D. E., 2008, *ApJ*, **688**, 709
- Verde L., Treu T., Riess A. G., 2019, *Nature Astronomy*, **3**, 891
- Villaescusa-Navarro F., et al., 2021, *ApJ*, **915**, 71
- Virtanen P., et al., 2020, *Nature Methods*, **17**, 261
- Vogelsberger M., Marinacci F., Torrey P., Puchwein E., 2020, *Nature Reviews Physics*, **2**, 42
- Wechsler R. H., Tinker J. L., 2018, *ARA&A*, **56**, 435
- Zentner A. R., Semboloni E., Dodelson S., Eifler T., Krause E., Hearin A. P., 2013, *Phys. Rev. D*, **87**, 043509
- van Daalen M. P., Schaye J., 2015, *MNRAS*, **452**, 2247
- van Daalen M. P., Schaye J., Booth C. M., Dalla Vecchia C., 2011, *MNRAS*, **415**, 3649
- van Daalen M. P., McCarthy I. G., Schaye J., 2020, *MNRAS*, **491**, 2424
- van Loon M. L., van Daalen M. P., 2024, *MNRAS*, **528**, 4623

APPENDIX A: MASS DISTRIBUTION PLOTS

We give here some extra mass distribution plots for some of the different probes we used in section 3.1.1. Figures A1 and A2 show the same distributions for 2 different overdensity regions. Each figure consists of 6 panels that contain a combination of two of the following mass distributions; the outliers for the difference of the mass profiles of the haloes from the average mass profile, the outliers of the distance of the centre of potential for the dark matter only simulation from the centre of potential for the fiducial simulation, the outliers for the values of f_{ret} , and all the haloes. All the outliers are defined as being 2σ away from the average value of the distribution. All the distributions are normalized to make them easier to compare.

One interesting result that comes from these figures is the secondary peak in the mass distribution of the haloes that are outliers in the mass profiles, in fig. A2 which is for the $500\rho_c$ region, the smallest of the 2. This is interesting because it is something we would expect if this selection of haloes included many cases of centre misalignment. As we have already discussed, displacing the centre position will lead to a smaller mass, especially for small regions around the centre, as we are now sampling from a less dense region. If there are many such cases in a selection of haloes, it would lead to a secondary peak in mass values lower than the main peak of the distribution, which will disappear in the same distribution for larger regions. This is indeed what we observe in these results.

APPENDIX B: MASS FRACTION PLOTS

In this appendix, we give the plots for the mass fractions which were not included in section 3.2. In each of the figures below, we show f_{ret} as a function of f_{bc} for different overdensity regions. We have two panels, on the left we have the results by taking into consideration all the haloes of the simulation, without any halo cuts. On the right panel, we show the results after cutting the haloes that were identified as outliers using the distance between the centre of potential and the centre of mass, as we have discussed in section 3.1. For the fitting, we use eq. (26) and the values of the fitting parameters can be found in tables 4 and 5 for the figures without and with the halo cuts respectively. The legends are identical to figs. 11 and 12 and therefore not included.

In figs. B1 and B2 we have the results for the R_{50c} and R_{100c} regions. These regions are relatively large and the results are very similar to each other and with the ones for the R_{200m} region which is shown in fig. 11. There is no improvement with the cuts for centre misalignment, there is however a noticeable change on the f_{ret} values which makes a difference in the fitting. For figs. B3 and B4, where we have the results for the R_{200c} and R_{1000c} regions, we see a noticeable improvement on the error bars when we exclude the centre of mass outliers. This leads to a more reliable fit. We also notice how in fig. B4, for high values of f_{bc} , f_{ret} no longer seems to follow the relation described in eq. (26).

Lastly in fig. B5, where we have the results for the smallest region we studied (R_{2500c}), we see that the fit is not great in both panels. This is because the region is so small that it is very susceptible to noise, and the exclusion of potential cases of centre misalignment did not improve the fit. Despite the problems with the fit, we can still say that the fitting relation can describe the general trend, but not to a high accuracy.

APPENDIX C: POWER SUPPRESSION PLOTS USING ONE REGION WITH HALO CUTS

The plots for the model results with the halo cuts (as described and analyzed in section 3.1) are given in this appendix. In section 3.4.1 we have included the results for the fiducial simulation using the regions R_{200m} , R_{200c} and R_{500c} for the halo definition. Here we include the results for the R_{50c} , R_{200m} , R_{1000c} and R_{2500c} regions (figs. C1 and C2). We also include the results using the two largest regions (R_{50c} , R_{100c}) for the simulation using strong jets. Each figure has 2 panels for different combinations of simulation and region, with the appropriate caption.

For the fiducial simulation, by using different simulations we are able to accurately probe different scales. For the R_{50c} region, which is the largest one, we can see that we have a better match for the large scales compared with all the others. The R_{100c} region is able to accurately match the scales around 2 to 3 h/Mpc but has a worse match in both the large and small scales. Finally for the last two regions (R_{1000c} and R_{2500c}) we have a worse match in all scales. The reason for that is the fitting of f_{ret} with f_{bc} , which is not very accurate for these small regions. As a result, the model is not able to properly scale the power spectra.

In section 3.4.2 we analyzed the results for all the different simulations (see fig. 19). From all the simulations we used, the worst performance was for the strong jets simulations. One hypothesis was that the matter ejected from the haloes goes to greater distances than in other simulations and therefore we need a bigger region to more accurately probe the power suppression in the large scales. In fig. C3 we see the one-region results for R_{50c} and R_{200m} . As we can see, even with the slight increase in the radius for R_{50c} we do not see a clear improvement from R_{200m} . Of course, the difference in the radius between the two might not be enough to improve the results, and testing for larger regions might show better results.

APPENDIX D: POWER SUPPRESSION PLOTS USING ONE REGION WITHOUT HALO CUTS

Similar to the previous appendix, we include here the model results, without the halo cuts. We include the exact same combinations of simulations and regions. The models for the fiducial simulation, using the different regions are shown in figs. D1 and D2. The plots for the strong jets simulation using the R_{50c} and R_{200m} regions are shown in fig. D3.

One thing we notice when we are looking at the results for the fiducial simulation is that they show an improvement over the corresponding results using the halo cuts. With the exception of the R_{2500c} region, which shows really poor results in either case, all other regions show either a slight or more noticeable improvement. This confirms our findings in section 3.4 where we discussed possible reasons that explain this improvement.

For the strong jets simulation, the results in fig. D3 are very similar to each other and with the ones with the halo cuts in appendix C. This confirms that the sample bias was not the reason for the poor (compared with all the other simulations) match between the true and modelled power suppression. This mismatch is caused by the peculiarities of this simulation, which we have already discussed.

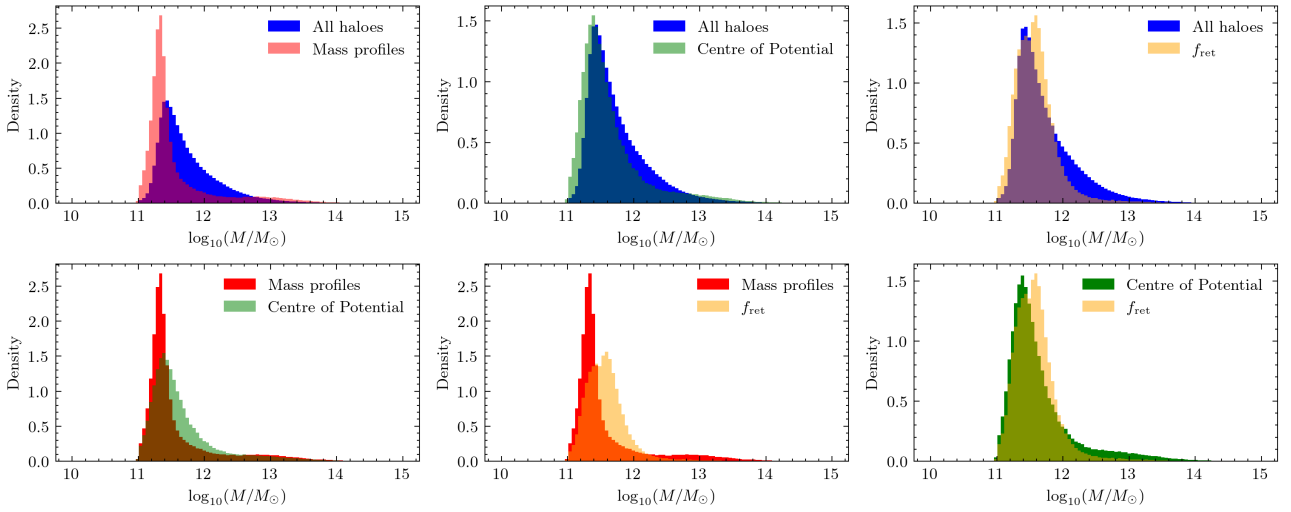


Figure A1. Distribution histograms for the overdensity region of $200\Omega_m\rho_c$.

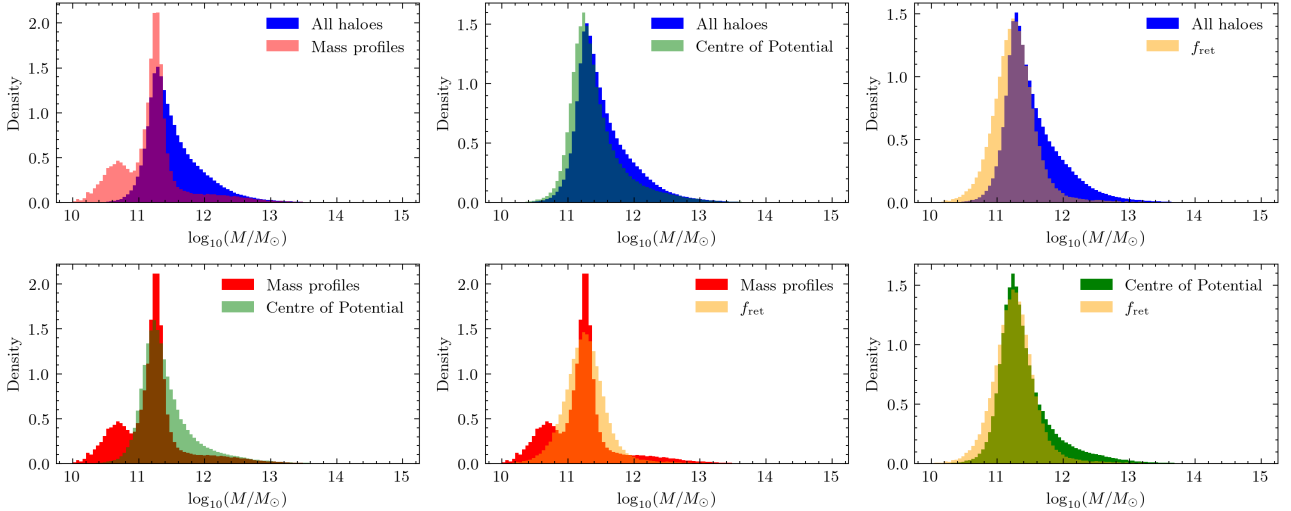


Figure A2. Distribution histograms for the overdensity region of $500\rho_c$.

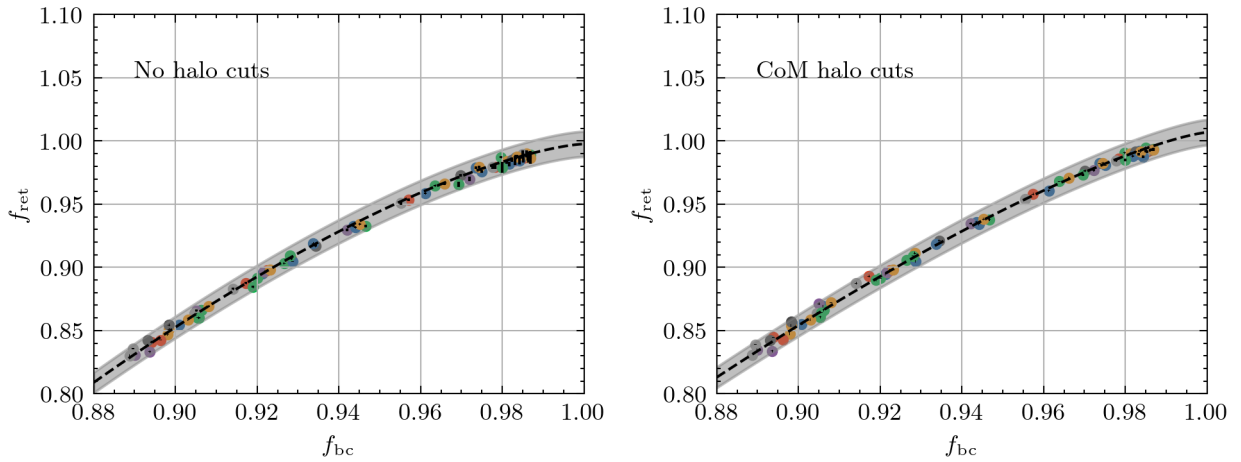
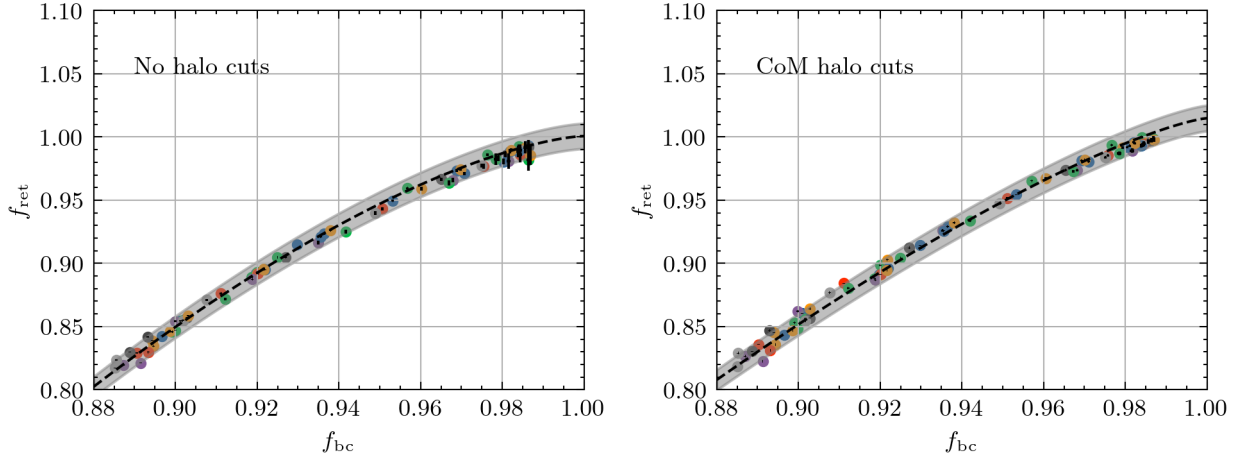
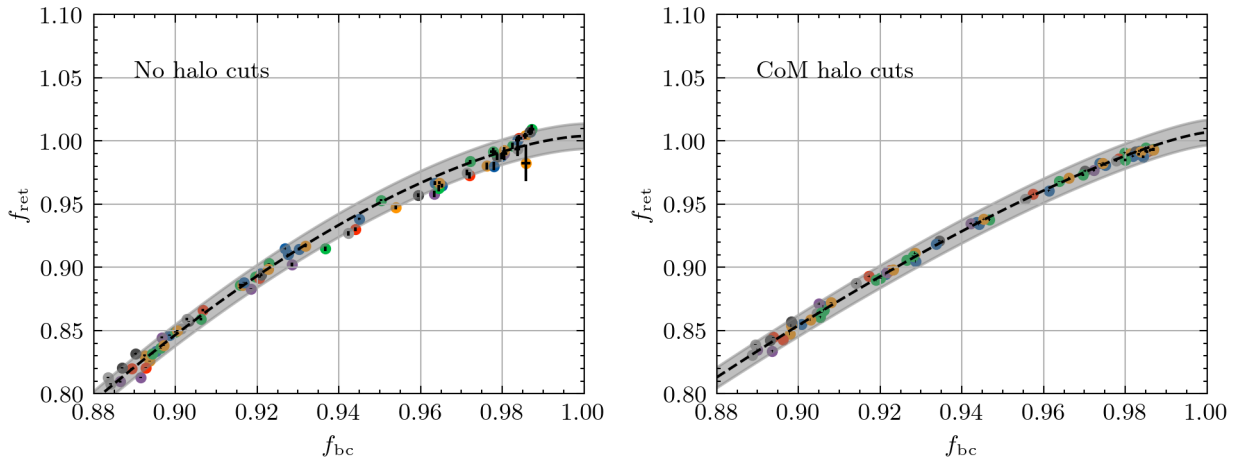
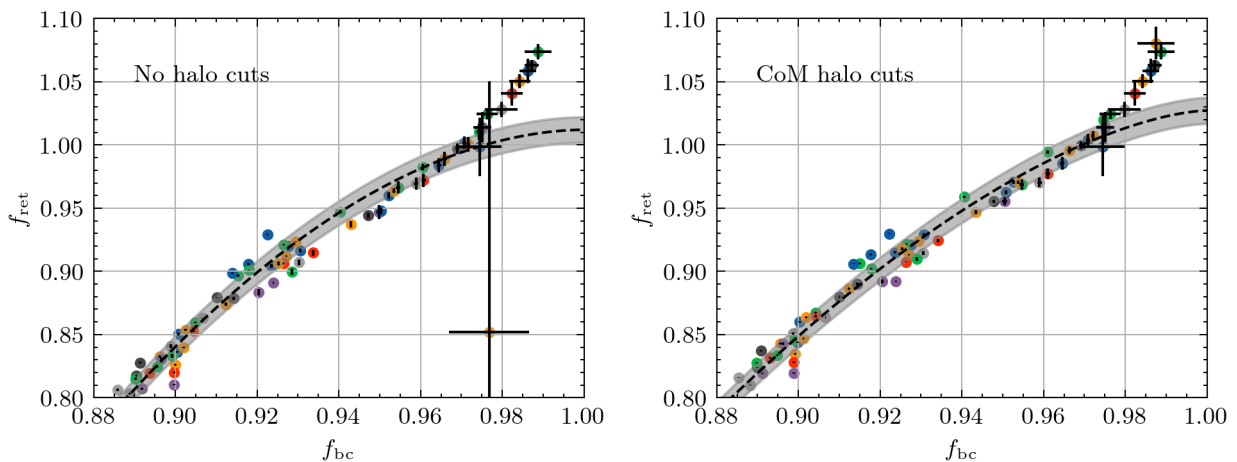


Figure B1. f_{ret} as a function of f_{bc} for the R_{50c} overdensity region.

**Figure B2.** f_{ret} as a function of f_{bc} for the R_{100c} overdensity region.**Figure B3.** f_{ret} as a function of f_{bc} for the R_{200c} overdensity region.**Figure B4.** f_{ret} as a function of f_{bc} for the R_{1000c} overdensity region.

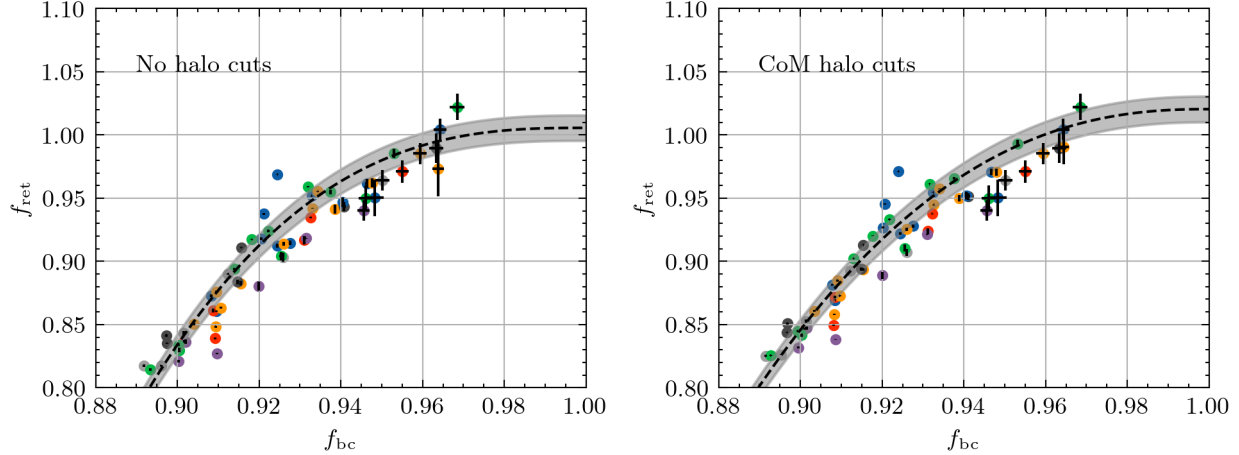


Figure B5. f_{ret} as a function of f_{bc} for the R_{2500c} overdensity region.

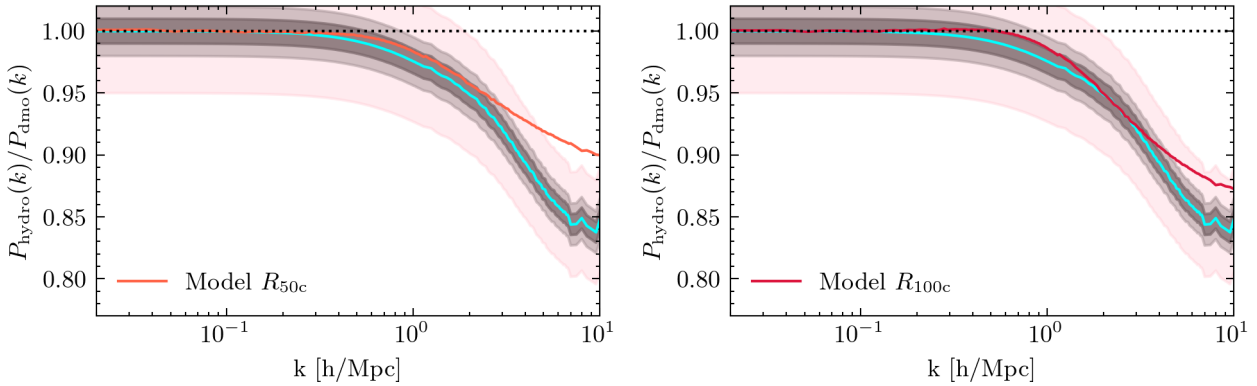


Figure C1. Left panel: fiducial R_{50c} . Right Panel: fiducial R_{100c} .

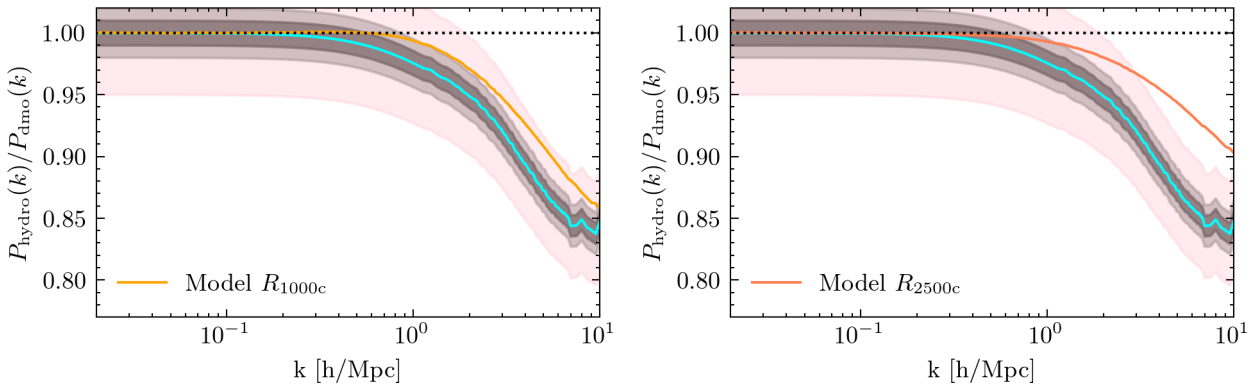
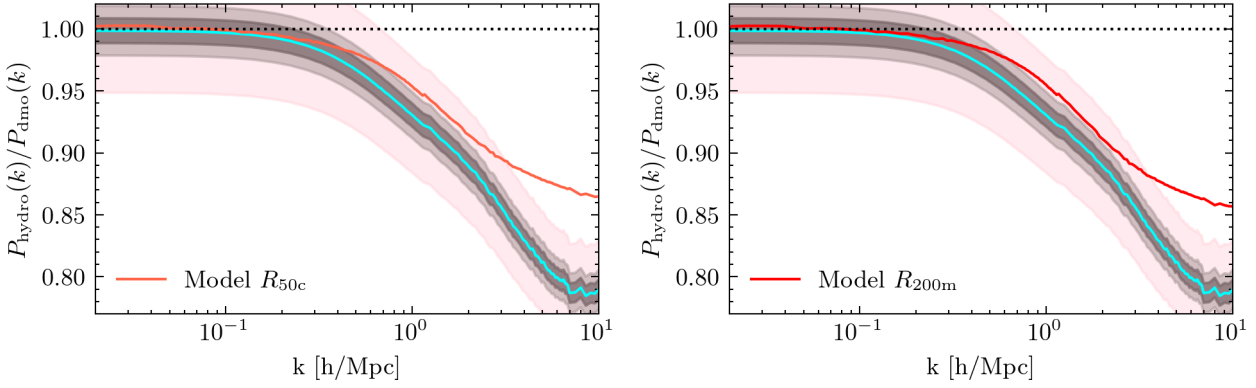
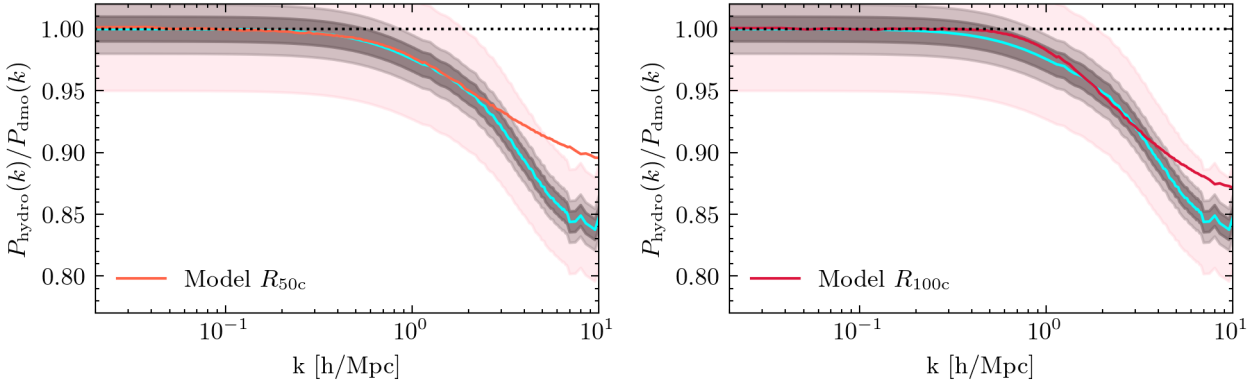
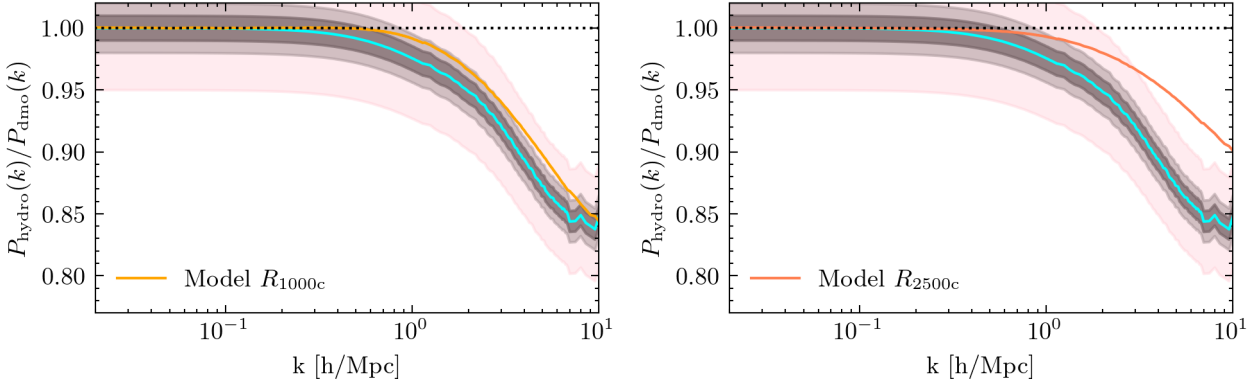


Figure C2. Left panel: fiducial R_{1000c} . Right Panel: fiducial R_{2500c} .

**Figure C3.** Left panel: strong jets R_{50c} . Right Panel: strong jets R_{200m} .**Figure D1.** Left panel: fiducial R_{50c} . Right Panel: fiducial R_{100c} .**Figure D2.** Left panel: fiducial R_{1000c} . Right Panel: fiducial R_{2500c} .

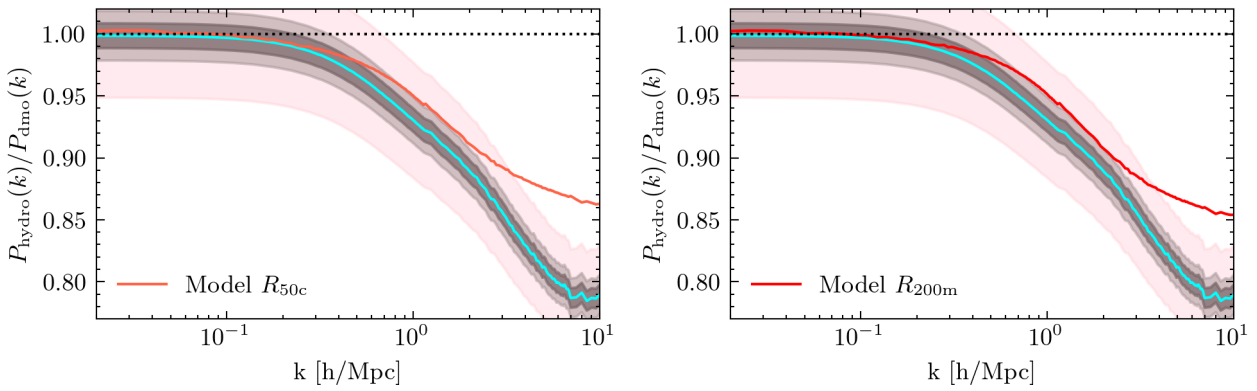


Figure D3. Left panel: strong jets R_{50c} . Right Panel: strong jets R_{200m} .